Rockwall permafrost dynamics evidenced by Repeated and Automated Electrical Resistivity Tomography at Aiguille du Midi (3842 m a.s.l., French Alps)

Feras Abdulsamad[1], Josué Bock[1], Florence Magnin[1], Emmanuel Malet[1], André Revil[1], Matan Ben-Asher[1], Jessy Richard[1, 2], Pierre-Allain Duvillard[2], Marios Karaoulis[3], Thomas Condom[4], Ludovic Ravanel[1] and Philip Deline[1]

1. EDYTEM, CNRS - Université Savoie Mont-Blanc, 73370 Le Bourget du Lac, France
2. Naga Geophysics, 229 rue Joseph Fontanet 73000 Chambéry, France
3. School of Geology, Geophysics Department, Aristotle University of Thessaloniki, Thessaloniki, Greece
4. Univ. Grenoble Alpes, IRD, CNRS, INRAE, Grenoble-INP, IGE, 38000 Grenoble, France

Corresponding author: Abdulsamad Feras (feras.abdul-samad@univ-smb.fr)

Emails: feras.abdul-samad@univ-smb.fr; andre.revil@univ-smb.fr; ludovic.ravanel@univ-smb.fr; florence.magnin@univ-smb.fr; mkaraoulis@geo.auth.gr; matan.ben-asher@univ-smb.fr; pierre-allain.duvillard@naga-geophysics.com; josue.bock@laposte.net; emmanuel.malet@univ-savoie.fr; jessy.richard@naga-geophysics.com; thomas.condom@ird.fr; philip.deline@univ-smb.fr

Keywords: Rockwall permafrost dynamics; Active layer thickness; Electrical resistivity tomography; Temperature measurements.

Intended for publication in The Cryosphere

Abstract. Permafrost ~~warming~~ degradation significantly affects the stability of rockwalls in high altitude regions. Subsurface monitoring of rockwall permafrost temperatures is essential ~~to~~ for assessing ~~assess the resulting~~ potential geohazards. However, borehole temperature measurements generally lack of spatial representativeness in such highly heterogeneous ground conditions. This study investigates the permafrost dynamics and hydrogeological system at Aiguille du Midi (3842 m a.s.l., French Alps) using repeated and~~an~~ Automated-Electrical Resistivity Tomography (A-ERT) approaches, covering~~conducted over~~ a period of almost four years (06/2020-12/2023). A total of three geophysical profiles have been installed on three ~~sides~~ faces of the Aiguille du Midi (N-W, S and E). An autonomous acquisition system for permanent resistivity monitoring and remote data acquisition is implemented. ~~The site consists of rockwall massive and fractured granite, with infrastructures inside and water infiltration observed in the tunnels.~~ A time-lapse inversion technique is employed to get the temporal and spatial ~~time lapse~~ variations of the electrical resistivity ~~of Aiguille du Midi~~ at ~~different time scales~~seasonal and interannual time scales. ERT showed significant variations in the active layer thickness across different rock faces, along with a slight decrease in the resistivity at depth, indicating permafrost warming over time. There is no clear evidence of water infiltration or accumulation observed in the ERT results. Using a petrophysical model based on laboratory measurements of the thermal dependency of electrical resistivity, the temperature distribution within the frozen zone can be estimated from the resistivity measurements (under favorable condition at surface). Its comparison with direct temperature monitoring data in a 10-m depth borehole nearby the NW profile allows a quantitative evaluation of the modelled temperature revealing an accuracy of ~±1 °C. ~~In addition to the field measurements, laboratory measurements of electrical resistivity are conducted on one water-saturated granite sample in both unfrozen and frozen conditions to evaluate the temperature-dependency of resistivity. Temperature information about the thermal state of permafrost is available from three shallow boreholes drilled in 2009, used to validate~~

~~our interpretation. A-ERT showed significant variations in the active layer thickness across different rock faces, along with a slight decrease in the resistivity of permafrost, indicating its warming over time. Our findings indicate that the temperature dependence of resistivity in field conditions (open system) is slightly less pronounced than in controlled laboratory experiments (closed system). Using a petrophysical model connecting temperature to resistivity, the temperature distribution within the frozen zone can be estimated from the resistivity measurements (during summer and autumn) with an accuracy of ~±1 °C.~~ This research underscores the efficacy of ERT as a promising, non-invasive tool for monitoring permafrost dynamics in Alpine environments. It also reveals challenges associated with conducting A-ERT in high mountain environment, where the contact resistance is very high (~500 kΩ) and sometimes intermittent due to factors such as thunder strikes and rockfalls. ~~It highlights the need for further methodological refinement to better resolve subsurface properties, potentially using induced polarization data.~~

1. Introduction

Climate change accelerates the degradation of the permafrost~~cryosphere~~ in high-mountains areas worldwide (Smith et al., ~~Etzelmüller et al.,~~ 202~~0~~2). In the European Alps, permafrost has warmed up to > 1°C at 10 m depth, especially in bedrock permafrost (Etzelmüller et al., 2020; Magnin et al., 2024; Noetzli et al., 2024). Over the last decade, there has been a continuous increase in rockfall events, particularly those ~~affecting~~ impacting permafrost in the European Alps (Cathala et al., 2024; Jacquemart et al., 2024; Ravanel et al., 2017). Infrastructures located in high altitude are increasingly affected by these events (~~Offer~~

et al., 2025; Duvillard et al., 2021, 2018; Hartmeyer et al. 2020). Permafrost degradation/warming of the rock mass can also locally be accelerated by heat advection through water infiltration in fractures, causing the erosion of the ice-infill (Hauck and Hilbich, 2024; Hartmeyer et al. 2020). As a result, a loss of bonding between rock and ice may occur, which in turn alters changing in turn the mechanical properties of such assemblage (Mamot et al., 2018; Krautblatter et al., 2013). Therefore, Understanding the thermohydrological dynamics of steep Alpine rock faces is essential for assessing potential geohazards associated with permafrost degradation.

To assess permafrost warming, one approach is to directly determine and monitor Rrockwall temperatures can be directly determined and monitored using temperature sensors installed at the rock surface or in boreholes (*e.g.*, Magnin et al., 2024). AlthoughWhile borehole temperature monitoring is still the only direct method to detect the occurrence of permafrost, it provides only point-scalelocal information, while its distribution and evolution can be highly variable in extreme topographical conditions. That said, permafrost dynamic can be controlled by various processes such as water flows in fractures, that are not fully captured by point-scale temperature measurements (Hauck and Hilbich, 2024). In addition, boreholes in rockwall at high altitude are logistically difficult to realize. They are also expensive and invasive.

On the other side, Ggeophysical measurements provide higher spatial coverage with respect to boreholes. Various non- or minimally intrusive methods have been applied to evaluate permafrost, including Refraction Seismic Tomography (RST) (*e.g.*, Steiner et al., 2019; Draebing 2016), Ground Penetrating Radar (GPR) (Campbell et al., 2018), Electrical Resistivity Tomography (ERT) (*e.g.*, Mollaret et al., 2020; Krautblatter and Hauck 2007) and Induced Polarization (IP) (Maierhofer et al., 2024; Abdulsamad et al., 2019; Duvillard et al., 2018; Doetsch et al., 2015). Combined geophysical methods can take advantage of the complementary petrophysical and spatial sensitivities of these different methods. For instance,

ERT measurement was combined with RST to evaluate ice, air, water, and rock contents (Mewes et al., 2017; Hauck et al., 2011). Recently, joint inversion of ERT and RST could reduce the uncertainties in the evaluation of air, water, ice and rock contents (Pavoni et al., 2023; Steiner et al., 2021; Mollaret et al., 2020; Wagner et al., 2019). IP measurements (providing tomograms of the electrical conductivity and normalized chargeability) have been recently used to assess the distribution of permafrost temperature, relying on laboratory calibration and a petrophysical (physics-based) model connecting resistivity and normalized chargeability with temperature under frozen and unfrozen conditions (see Moser et al., 2025; Duvillard et al., 2021, 2018, and references therein).

In the last ~~few years~~two decades, ERT has become an increasingly popular tool in permafrost studies (*e.g.*, Herring et al., 2023; Farzamain et al., 2020; Magnin et al., 2015a; Krautblatter et al., 2010). Herring et al. (2023) provide a review of the use of ERT method in permafrost research, detailing both the advantages and limitations of this method in such a context. A significant advantage of using electrical resistivity measurements to assess mountain permafrost is that the freezing and thawing of water filling pores are associated with considerable changes in resistivity (generally between one to three orders of magnitude, see Coperey et al., 2019). Because of this sensitivity, electrical resistivity tomograms can be used to assess of the presence and distribution of permafrost.

Repeated ERT measurements at specific time intervals using the same survey geometry can be used to track the temporal and spatial evolution of permafrost over time (*e.g.*, Offer et al., 2025, Hilbich et al., 2008). However, rapid changes due to water flux, infiltration or drainage (such as during snowmelt or rainfall) may not be captured by monthly or seasonally repeated measurements (Krautblatter et al., 2010). Alternatively, continuous resistivity measurements, known as Automated-ERT (A-ERT) or ERT monitoring, offer the ability to track the ongoing evolution of permafrost and capture rapid, heterogeneous and non-linear

changes in its temperature and ice content (*e.g.*, Scandroglio et al., 2021; Doetsch et al., 2015). A-ERT over period of several years has been recently used to track the degradation of permafrost associated with global warming (Mollaret et al., 2019; Keusching et al., 2017; Doetsch et al., 2015; Hilbich et al., 2008).

Furthermore, the time-lapse inversion of geophysical data derived from fixed monitoring network provides a succession of tomograms showing the spatial and temporal changes in subsurface resistivity (see; Karaoulis et al., 2013; Loke, 1999). The r~~R~~esults of time-lapse inversions of apparent resistivity data can be directly linked~~related~~ to the evolution of permafrost throughout ~~during~~ the annual ~~yearly~~ cycle or to rapid variations caused by water infiltration or drainage during short periods of time (Keusching et al., 2017; Hilbich et al., 2008).

That said, A-ERT at high altitudes (>3500 m) and over a multi-profile setting has not yet been tested for pluriannual~~long term~~ permafrost monitoring. The use of A-ERT under high-altitude conditions presents specific challenges due to extreme topographical and climatic conditions as well as~~and~~ meteorological events. However, it could provide valuable information about the hydrogeological system and ~~the~~ evolution of permafrost in environments where its distribution and dynamic are highly heterogeneous.

In this study, we present the results of an A-ERT survey conducted over nearly four years (2020-2023) at Aiguille du Midi (AdM) in the Mont-Blanc massif (French Alps). The site consists of massive and fractured granite and includes infrastructures such as tunnels and elevators. Water infiltration was observed at various locations within the tunnels. The objective of this study is to investigate~~examine~~ permafrost dynamics from infra-seasonal to multiyear timescales and through various rock faces of a same site. Our goals include: (1) evaluating the potential of A-ERT to characterize permafrost dynamics, its heterogeneity and non-linearity in steep alpine rockwalls; (2) assessing the accuracy of temperature derived from resistivity

measurements; and (3) studying the hydrogeological system, including water infiltration and drainage in fractures, along with their thermal impacts. For this objective, a total of three ~~155-m-long~~ profiles were deployed downwards from the summit in three directions: North-West (NW), South (S) and East (E). Each profile consists of 32 electrodes spaced at 5 m. In addition to field data, laboratory resistivity measurements were conducted on granite core sample, in both unfrozen and frozen conditions. Furthermore, temperature which was continuously monitored in a 10 m deep borehole along the NW profile is used to quantitatively evaluate the temperature estimation using ~~three shallow boreholes, one of them is located along the ERT profile, is used to validate our interpretation of the~~ geophysical measurements of electrical resistivity.

2. Study site

We investigate the ~~iconic~~ Aiguille du Midi (3842 m a.s.l.), which is the highest and most western summit of the Aiguilles de Chamonix (Fig. 1a). It is located on the NW~~north-west~~ flank of the Mont-Blanc massif ~~(Fig. 1a)~~. It includes three peaks that are all connected by human-made bridges and galleries. In average, AdM is visited in summer by around 5000 visitors a day transported from the city of Chamonix by cable-cars. The appearance of the summit of AdM has been greatly affected by the construction and developments carried out since the 1950s (see Fig. 1). Our study focuses on the central peak, which is the highest among the three, and which hosts the cable-car station connecting AdM to Pointe Helbronner with the *Panoramic Mont-Blanc* cable car. The topography is characterized by vertical rock walls with an average slope of 78° on the North-West face.

The lithology in the study area is dominated by massive granite with a very low porosity (~ 0.01, Magnin et al., 2015a). The highest parts (3740 to 3840 m a.s.l.) of the peak tend to be steep, contain few large fractures, and, in places, are characterized by vertical foliation bands and small cracks (Magnin et al., 2015b). Figure 2 shows the mean monthly and annual air

temperature at AdM during the study period. The year 2021 was the coolest year (yearly averages: -5.8 °C, -6.9 °C, -5.3 °C, and -5.7 °C from 2020 to 2023, respectively).

In order to evaluate the thermal state and the distribution of permafrost at AdM, three boreholes have been drilled in 2009. They are labeled BH-NW on the NW face, BH-S on the South face and BH-E on the East face. Each borehole is 10-m-deep and 66 mm in diameter, and waswere drilled normal to the topography (their position is shown in Fig. 1b-d). Each borehole is equipped with 15-thermistor strings calibrated in an ice-water bath and then placed at different depths in the borehole. In the past few years, the temperature of the permafrost core has shown significant variability is highly variable from one face to another. For example, at a depth of 10 meters, the temperature is approximately -4 °C on the NW face, while it is around -1 °C on the sun-exposed S face , with temperature of about −4 °C at 10 m depth of the NW face to −1 °C at the same depth in the sun-exposed (S face) (Magnin et al., 2024). Theose temperature differences indicate the presence ofmply strong temperature gradients within the rock mass. In the same way, the –Active Layer Thickness (ALT, *i.e.*, the maximum seasonal thaw layer that derived from temperature measurements) is also highly variable as interpolated between temperature sensors: it is observed to be around 1.6 3 to 2.7 m at the end ofin summer on the NW side, while it reaches 46.8 to 7.6 m on the S side in the early fall. Below this depth, permafrost is present all along the year (see details in Magnin et al., 2024). Figure A1 (appendix A) shows the temperature variation over depth in boreholes BH-NW and BH-S on different date.

BH-NW is located along an electrical resistivity profile (NW profile) and is positioned between electrodes 8 and 9 (counted from the bottom) of the NW profile (see Fig. 1c). The temperature measured in this borehole is used to assess the accuracy of the temperature derived from ERT results using the petrophysical model presented in the next section.

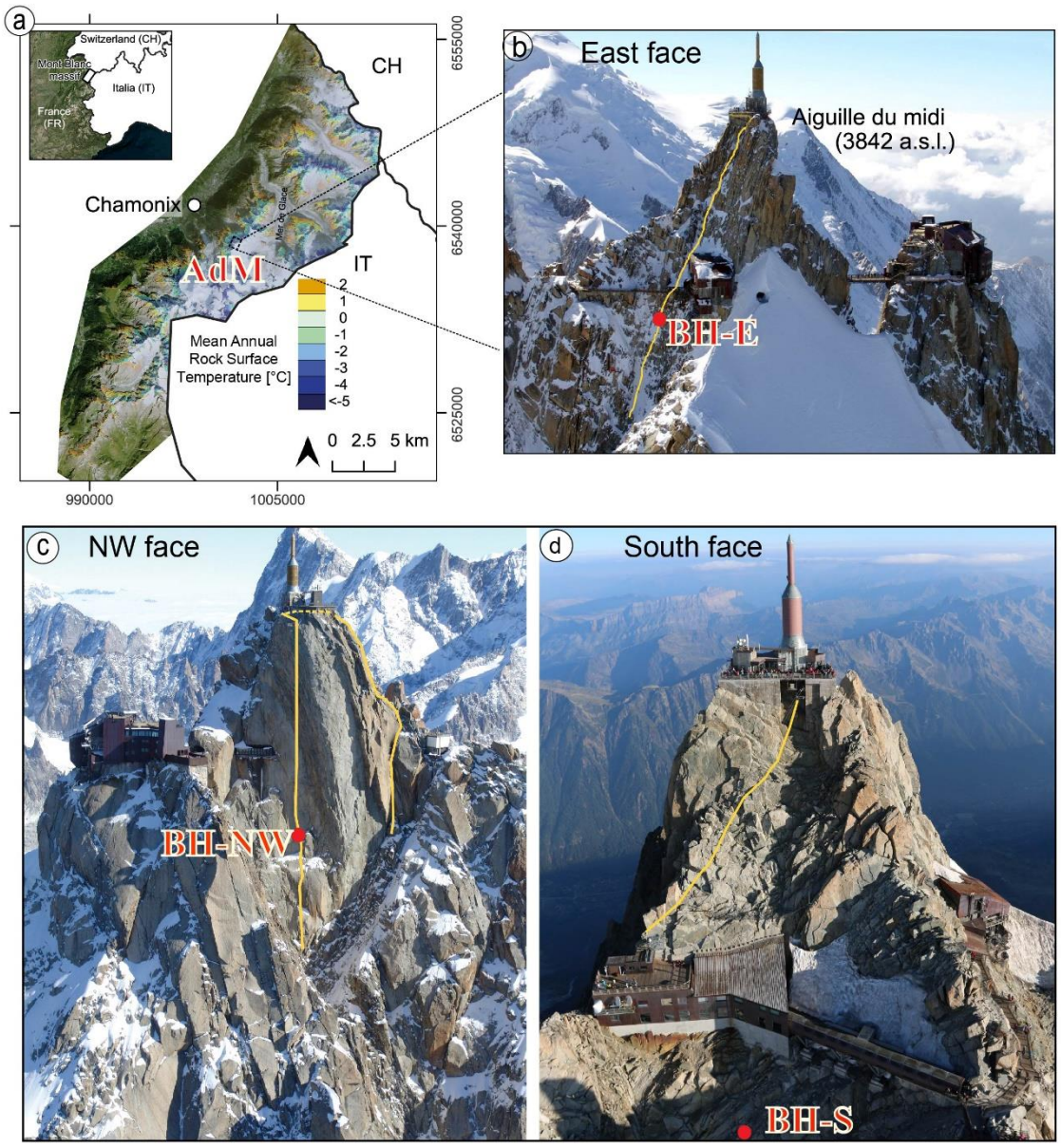

Figure 1. Study site location and geophysical survey setting. The yellow lines indicate the approximate positions of electrical resistivity profiles on each side (NW, E and S profiles). The red dots denote the borehole locations. (a) Location of the study site (Aiguille du Midi (AdM)), in the Mont Blanc massif (here, the French side) largely affected by the permafrost (from, Magnin et al. (2015b)). ~~(b)~~ The electrical resistivity profile and borehole locations at the East face (b), ~~. (c) The electrical resistivity profile and borehole locations~~ at the North-West face (c) and ~~. (d) The electrical resistivity profile and borehole locations~~ at the South face (d).

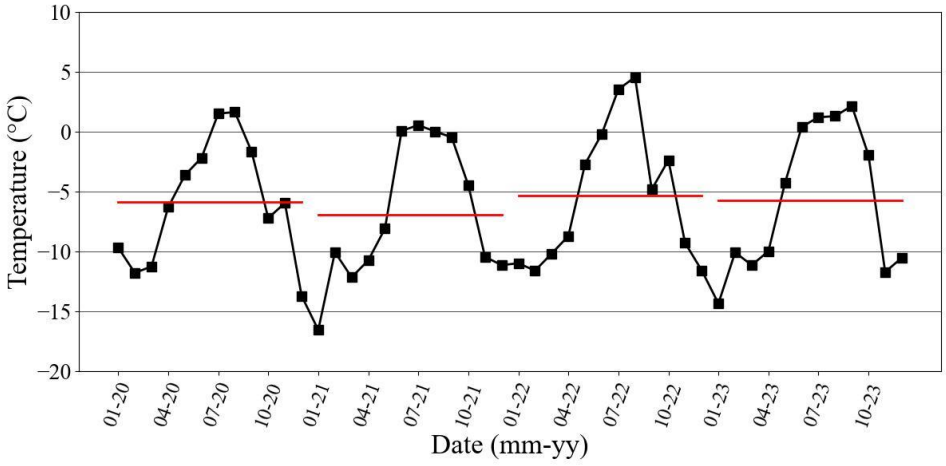

Figure 2. Monthly average air temperature (°C) at AdM during the survey period (Data from the meteorological station of Institute of Environmental Geosciences at the Aiguille du Midi). Horizontal bars show the annual average air temperature.

3. Electrical conductivity - temperature relationship

The electrical conductivity of a rock represents its ability to conduct an electrical current under the application of an imposed electrical field. The electrical conductivity (inverse of the electrical resistivity) of a rock depends on its porosity ϕ (dimensionless), water content θ (dimensionless), pore water conductivity, Cation Exchange Capacity (CEC), and rock temperature T (in °C) (*e.g.*, Revil et al., 1998).

Above the freezing point (typically, but not necessary, around 0°C), electrical conductivity ($\sigma(T)$ in S m^{-1}) increases linearly with temperature according to Revil et al. (1998):

$$\sigma(T) = \sigma(T_0)\left[1 + \alpha_T (T - T_0)\right], \qquad (1)$$

where α_T = 0.021±0.02 °C^{-1}, T_0 = 25°C denotes the reference temperature, and $\sigma(T_0)$ denotes the conductivity of the rock at the reference temperature.

In contrast, under freezing conditions, temperature variations have a significant influence on electrical conductivity because of the occurrence of an insulating phase (*i.e.*, ice formation) in the pore space and despite the increase in the salinity of the pore water with

temperature decrease. This temperature dependence of electrical conductivity can be modeled as follows (see details in Duvillard et al., 2021; 2018; Coperey et al., 2019):

$$\sigma(T) \approx \left[(\phi - \theta_r) \exp\left(-\frac{T - T_F}{T_C} \right) + \theta_r \right] \frac{\sigma(T_0)}{\phi} \left[1 + \alpha_T (T - T_0) \right], \quad (2)$$

Where θ_r (dimensionless) denotes the residual water content when T<<T_F, T_F denotes the liquidus or freezing point/temperature, T_C denotes a characteristic temperature controlling the transition between the unfrozen state and the frozen state, and $\phi - \theta_r$ denotes the maximum volumetric ice content at low temperatures. Equation (2) provides the opportunity to convert electrical conductivity or electrical resistivity tomogram measured in the field to a temperature distribution (*e.g.*, Duvillard et al., 2021).

4. Methods

4.1 Laboratory measurements

In order to calibrate our field measurements and ~~To~~ evaluate the parameters (*e.g.*, T_C, θ_r) in the petrophysical model discussed above (Section 3), ~~and to calibrate our field measurements,~~ we conducted an electrical conductivity experiment on a granite rock sample collected from an outcrop on the site. The cube-shaped granite sample (dimensions: 5×5×5 cm^3) ~~(cubic) core sample~~ was dried during 24 h at approximately~~around~~ 100 °C, then saturated under vacuum with degassed water. The water conductivity was measured to be 0.016 S m^{-1} (representative of the conductivity of collected water from ~~melted snow in~~ the field (about 150 µS/cm or 0.015 S m^{-1})) at equilibrium at T = 25˚C. The sample was left in the solution for several weeks to reach chemical equilibrium before performing the laboratory measurements. The Sample was characterized by a very low porosity ϕ = 0.014.

For thermal-resistivity analysis, ~~T~~the sample was placed ~~installed~~ in a heat-resistant insulating bag immersed in a thermostat bath (KISS K6 from Huber; dimensions: 210×400×546 mm^3; bath volume: 4.5 L). The temperature of the bath was controlled with a precision of 0.1 °C. Glycol was used as the heat carrying fluid (Coperey et al., 2019). The complex conductivity spectra were obtained over the temperature range of +10 to −10 °C, using a high-precision impedance-meter ZEL-SIP04-V02 (Zimmermann et al., 2008). The resistivity measurements reported here are at a frequency of 1 Hz (Coperey et al., 2019).~~.~~

~~For comparison,~~ Figure 3 presents the measurement results for the granite sample from the study site (labeled Sample AdM), alongside measurements of~~from~~ another granite sample (Sample Cosmiques) collected from a nearby site at the lower Cosmiques ridge (Mont-Blanc massif, 3613 m a.s.l.), as reported by Duvillard et al. (2021). The experimental datasets are presented along with data fits, using Equations 1 for temperatures above the freezing point, and Equation 2 for temperatures below the freezing point. We see that the model proposed in Section 3 is able to fit the data above and below the freezing temperature, providing a proxy for connecting electrical conductivity or electrical resistivity to temperature. ~~Furthermore, the Sample AdM was characterized by a very low porosity ϕ = 0.014.~~

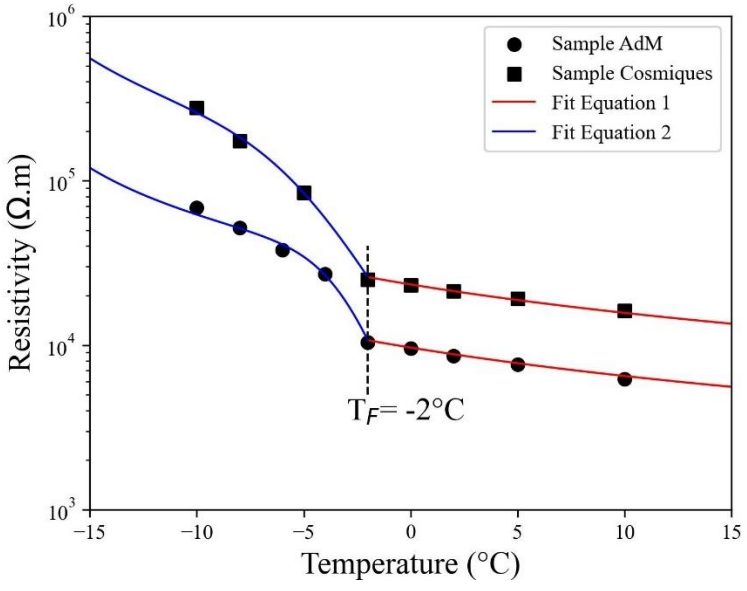

Figure 3. Resistivity-temperature relationship from laboratory measurements on two granite samples from (1) the study site (Sample AdM), and (2) from the Cosmiques ridge, Mont-Blanc massif, West (3613 m a.s.l.) (Sample labeled Cosmiques). T_F denotes the freezing temperature. The solid lines correspond to the fits using the Equation 1 (red lines) and Equation 2 (blue lines), in unfrozen and frozen conditions, respectively. The parameters of the model in Equation 2 are (T_C=-1.3 °C, θ_r=0.004, $\sigma(T_0)$ = 2.3×10^{-4} S m^{-1}) for Sample AdM, and (T_C= -2.17 °C, θ_r = 0.004, $\sigma(T_0)$ = 9.5×10^{-5} S m^{-1}) for Sample Cosmiques.

4.2 ERT Data acquisition

~~A~~ ERT has been conducted over a four-years period (06/2020 - 12/2023). A total of three cables, each with 32 take-outs spaced 5 m (for a profile length of 155 m), were installed. The three cables were deployed downwards from the summit in three directions: North-West (NW), East (E) and South (S). The S profile starts at the South side and pass to the North-West side around mid-distance (see Fig. 1c, d). The installation of cables was gradual (over a year) starting from NW side (installed in June 2020), then on the South side (installed in July and August 2020), and finally on the East side (installation finished in March 2021 because of snowpack in 2020 at this side). In order to ensure good electrical contact between electrodes and rock mass, stainless steel (A4/316) climbing bolts (Fischer 10×126 mm) poured in salty bentonite were used and placed firmly in holes drilled in the rock. A specially designed jumper was used to attach each take-out to the bolt to ensure maximum contact. ~~The electrodes remained embedded in the rock wall for all subsequent resistivity measurements.~~ The resistivity cables were attached to anchors to minimize damage from rockfall and snow pressure.

A LS2-Terrameter (ABEM) with internal impedance of 20 MΩ was used for the data acquisition ~~with internal impedance of 20 MΩ~~. The ERT device and control system for monitoring were deployed inside the summit station with network access, power connection, and overvoltage protection. Data acquisition was fully automated and remotely controlled. Finally, the position of every electrode was measured using a differential GPS when the signal is available and a theodolite in steep areas~~.~~. The measurements ~~themselves~~ were carried out

using a Wenner configuration ~~(voltage electrodes in between the current electrodes)~~, which provides ~~leads to~~ a high signal-to-noise ratio and is weifly used ~~largely applied~~ in mountain permafrost environments (Mollaret et al., 2020; Krautblatter and Hauck, 2007; Dahlin and Zhou, 2004). Each profile consists of 155 data points. An injected current ranging from 0.1 mA to 200 mA was applied, with a maximum stack numbre of 4 was applied to ensure a standard deviation of less than 5 % in the measured resistivity.

The first measurements were performed in June 2020. In the period June 2020 and September 2021, ERT measurements were repeated occasionally. Then the continuous measurements started in late September 2021 after developing an automated system of acquisition. Datasets were daily recorded for each profile (NW, S and E profiles).~~In the period June 2020 and September 2021, ERT measurements were repeated occasionally.~~ ~~A~~ A Contact Resistance (CR) test was performed before each series of measurements. A high contact resistance in the rock wall (>100 kΩ) was encountered throughout the entire survey period, which posed a challenge to the quality and continuity of data acquisition. ~~Figure 4 shows the evolution of contact resistance for each electrode over time for the NW and S profiles. We notice that~~ CR varies between a few kΩ and 10 000 kΩ. Figure B1 shows the temporal evolution of CR at profiles S and NW and the gaps in the A-ERT measurements ~~(see Fig. 4)~~. However, beyond a CR threshold, the ERT measurements lose their accuracy. Electrodes with high CR (>600 kΩ) are excluded automatically by the LS2, leading to gaps in the pseudo-section of apparent resistivity. Special efforts were made to reduce CR and improve the electrode/rock contact, including the addition of salty water, using copper electrodes and duplicate electrode. The latter one resulted in a significant and a durable improvement in RC (one order of magnitude reduction in CR).

The A-ERT ran into numerous software and hardware issues, resulting in unsystematic data gaps. The E face cable was severely damaged by a lightning strike, before being totally

destroyed by an uncontrolled rock purge. Additionally, NW and S cables were both damaged by rockfall, leading to significant data gaps (see Fig. 4).~~,~~ Repairing or replacing the damaged cables was not possible for several reasons (limited access to the cable path because of accumulated snowpack~~).).~~

~~Datasets were recorded for each profile (NW, S and E profiles) and two long profiles of 64 electrodes (*i.e.*, profile NW+E and profile NW+S).~~

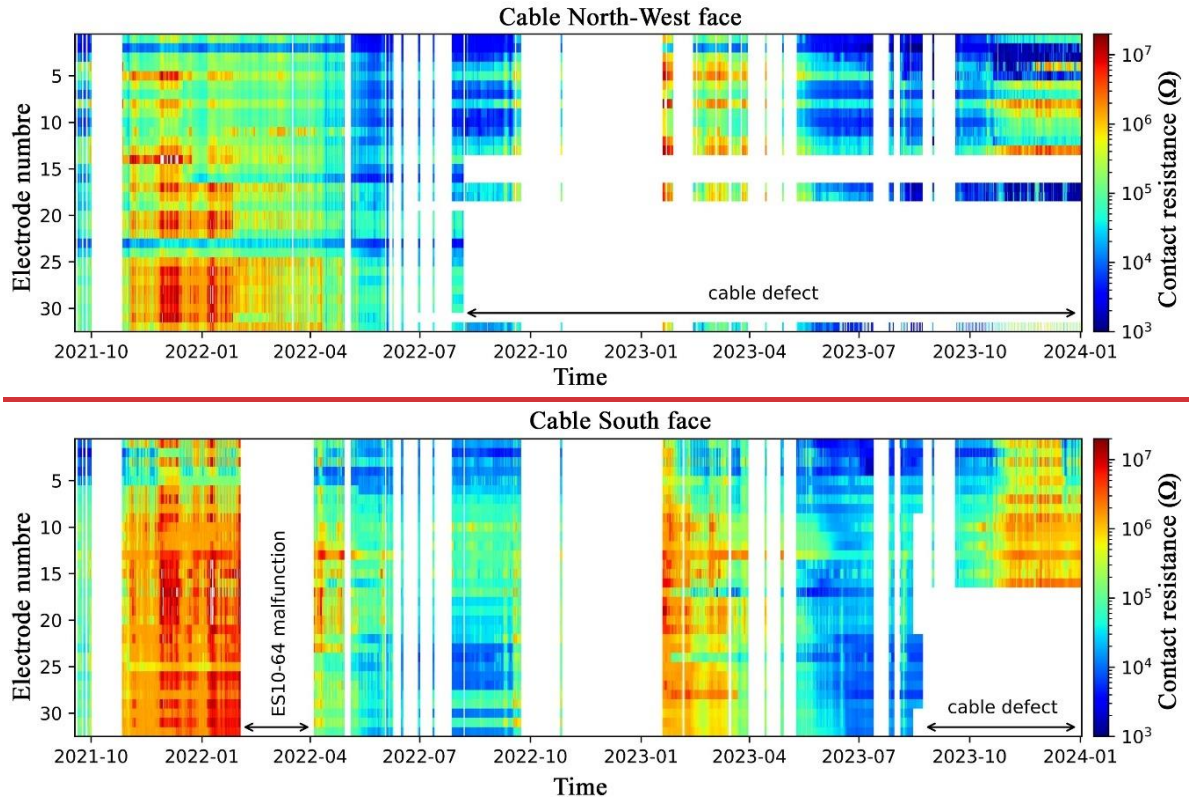

~~Figure 4.~~ ~~Temporal evolution of contact resistance at the North-West side and South side. Data partly missing are due to cable defects.~~

4.3. Data processing and inversion

The apparent resistivities were calculated using the open-source package pyGIMLI (Rücker et al., 2017), which combines measured resistances and lectrode positions. ~~As expected, data from A-ERT are of lower quality than manual measurements where the user can intervene to improve contact resistance after each electrode check (Doetsch et al., 2015; Hilbich et al., 2009). Furthermore, existing infrastructure with metal supports and the harsh topography of the site also affect data quality. The topography is characterized by vertical rock walls with an average slope of 78° on the North-West face, which posed some challenges in inversion software.~~ Figure 4 shows the temporal distribution of apparent resistivities measured along the S-profile, with examples (shown in different in colors) of time series of measured apparent resistivities obtained using various quadrupole configurations (AMNB).

The majority of measured apparent resistivities are distributed over three decades (100 Ω.m to 100 kΩ.m), with few data points out of this range.

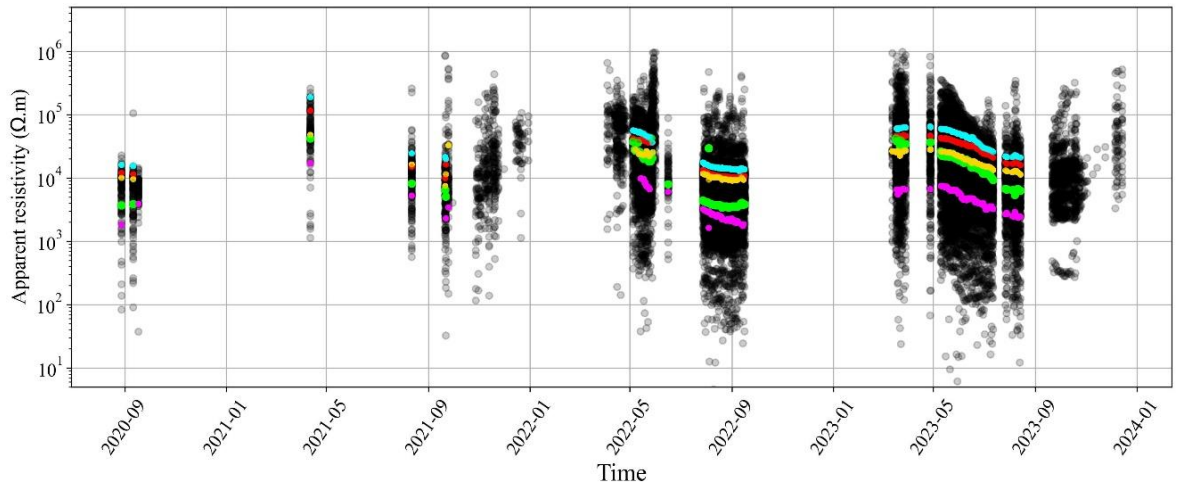

Figure 4. Distribution of apparent resistivity over time at the S face (~300 datasets). In color, examples of times series of resistivity measured with different quadrupoles.

For datasets used in inversion, the selected data were subjected to the following analysis. ~~Therefore, the first challenge was evaluating data quality and rejecting poor dataset.~~ The primary criterion was the number of connected electrodes. We tolerated up to four unconnected

electrodes (because of high RC) in a pseudo-section depending on their positions, as the contribution of electrodes is not equal in the pseudo-section. The datasets used in this study were selected from overall available data to support the objectives of this study. After selecting valid datasets, outliers within each pseudo-section were removed. For data filtering, we analyzed individually few pseudosections (at different times (summer, spring, etc…), as a result of this analysis we decided to apply filter outliers out of range (300Ωm - 20 kΩm) for data measured in summer and autumn, and out of range (300Ωm - 200 kΩm) for data measured in spring and winter. More data filtered at higher resistivities, where data quality is usually poor. Table 1 appendix C summarizes the data presented in this study. Most datasets have more than 80 % of the original recorded data points of each pseudo-section.

Table 1. summary of data presented in this study. Number of data before filtering is 155 datum points of Wenner configuration. Most of datasets has more than 80% of total number of measurements. Two datasets have more than 40% of lost data because of disconnected electrodes. The Data corresponds to the data of the data acquisition.

Date	**N-W Profile**		**S Profile**	
	Number of data after filter	Percentage (%)	Number of data after filter	Percentage (%)
30-06-2020	151	97.5	-	-
26-08-2020	149	96.1	90	58
17-09-2020	151	97.5	90	58
12-04-2021	118	76.1	121	78
09-07-2021	114	73.5	-	-
12-08-2021	149	96.1	140	90.3
17-09-2021	145	93.5	131	84.5
25-09-2021	143	92.2	144	92.9
29-03-2022	121	78	-	-
25-04-2022	141	91	131	84.5
14-05-2022	141	91	147	94.8
24-05-2022	140	90.3	146	94.1
30-06-2022	102	65.8	-	-
30-07-2022	-	-	145	93.5

~~15-08-2022~~	~~-~~	~~-~~	~~145~~	~~93.5~~
~~15-09-2022~~	~~-~~	~~-~~	~~144~~	~~93~~
~~19-03-2023~~	~~-~~	~~-~~	~~138~~	~~89~~
~~28-04-2023~~	~~-~~	~~-~~	~~143~~	~~92.2~~
~~25-05-2023~~	~~-~~	~~-~~	~~148~~	~~95.5~~
~~25-06-2023~~	~~-~~	~~-~~	~~144~~	~~92.9~~
~~29-07-2023~~	~~-~~	~~-~~	~~140~~	~~90.3~~

~~Furthermore, existing infrastructure with metal supports and the harsh topography of the site also affect data quality. The topography is characterized by vertical rock walls with an average slope of 78° on the North-West face, which posed some challenges in inversion software.~~

The inversion of the electrical resistivity datasets was performed using the open-source package pyGIMLI (Rücker et al., 2017; Günther et al., 2006). The inversion use~~d~~s a Gauss-Newton minimization algorithm of a cost-function penalizing the roughness of the electrical resistivity distribution on an irregular grid (Günther et al., 2006). In the absence of reciprocal dataset to estimate errors in measurements, we used a linear error model which assumed 5 % relative error and absolute error 1e5. The parameters used in the inversion process are zWeight = 10 and lambda =1. The inversion parameters zWeight was chosen higher than 1 to enhance the vertical discontinuities and structures (the active layer, and infrastructures), during the inversion process. An~~An~~ iterative process ~~analysis~~ was conducted to select the smoothness ~~regularization~~ parameter ~~s~~ that minimize~~s~~ the data misfit of individual inversions of ~~the~~a reference dataset ~~:~~

5. Results and interpretation

5.1. Overview of the raw data

Our interpretation of the ERT data starts ~~began with~~ with an analysis of the measured apparent resistivity data ~~(all selected data presented in this study before processing or filtering).~~ , which can~~This analysis can~~ provide insights into subsurface conditions. Figure ~~5~~5~~,~~ shows the variations ~~of~~in the average apparent resistivity ~~(*i.e.*, the average apparent resistivities~~ associated with the same electrode distance ~~(~~or pseudo-depth~~)~~ for three selected datasets from two profiles (NW and S profiles). The data reveal the interannual and seasonal variations in the measured apparent resistivity, as well as differences between the two sides. ~~in the pseudo-section), at different electrode distances or different depths of investigation.~~ During frozen conditions at the surface (dataset from 12-04-2021), the apparent resistivity is almost the same on both sides (~100 to 120 kΩm near the surface), with only a slight decrease with depth at both sides. In autumn, firstly, the resistivity values are higher in 2021 than in 2020 on both sides, which correlates with climatic data indicating that 2021 was a cooler year (see Fig. 2). Secondly, on the north face, the average resistivities increase with depth (from ~7 kΩ.m to ~12 kΩ.m), while on the south side, the average resistivities decrease with depth (approximately 13 kΩ.m at shallow depth to ~7 kΩ.m at greater depth). This difference in the trend between both sides could be interpreted by cooler conditions at north side and/or thicker active layer at the south face.

~~A difference can be observed between data on the S and NW profiles under unfrozen conditions (Fig. 5a and b). On the North-West face (NW profile) (Fig. 5a), the apparent resistivity is higher at depth (indicating frozen conditions) and lower near the surface (thawing conditions). In contrast, the South face (Fig. 5b) exhibits high values near the surface, related to the fractured area filled with air (resistive material), which increases the medium's resistivity, while lower values are found at greater depths due to close to 0°C conditions depicting warm~~

permafrost (*i.e.*, permafrost with temperature is > -2°C), or increased water saturation. In frozen conditions (Fig. 5c and d), a cooling effect is obvious near the surface on both sides. It is characterized by high apparent resistivity values (~120 kΩm) that decrease with depth.

Figure 6 shows the seasonal variation in the apparent resistivity over time of various electrodes quadrupoles (*i.e.*, at varying depths of investigation). Notably, data from the NW profile (a massive rock area) shows moderate variations over time. In contrast, the apparent resistivity variation is more significant at the Southern face (S profile), where a fracture zone may be filled with water, ice, or air throughout the year. Furthermore, the seasonal variation of apparent resistivity is more pronounced for shallow data (correlated with smaller distance between electrodes) on both sides (see further discussion below).

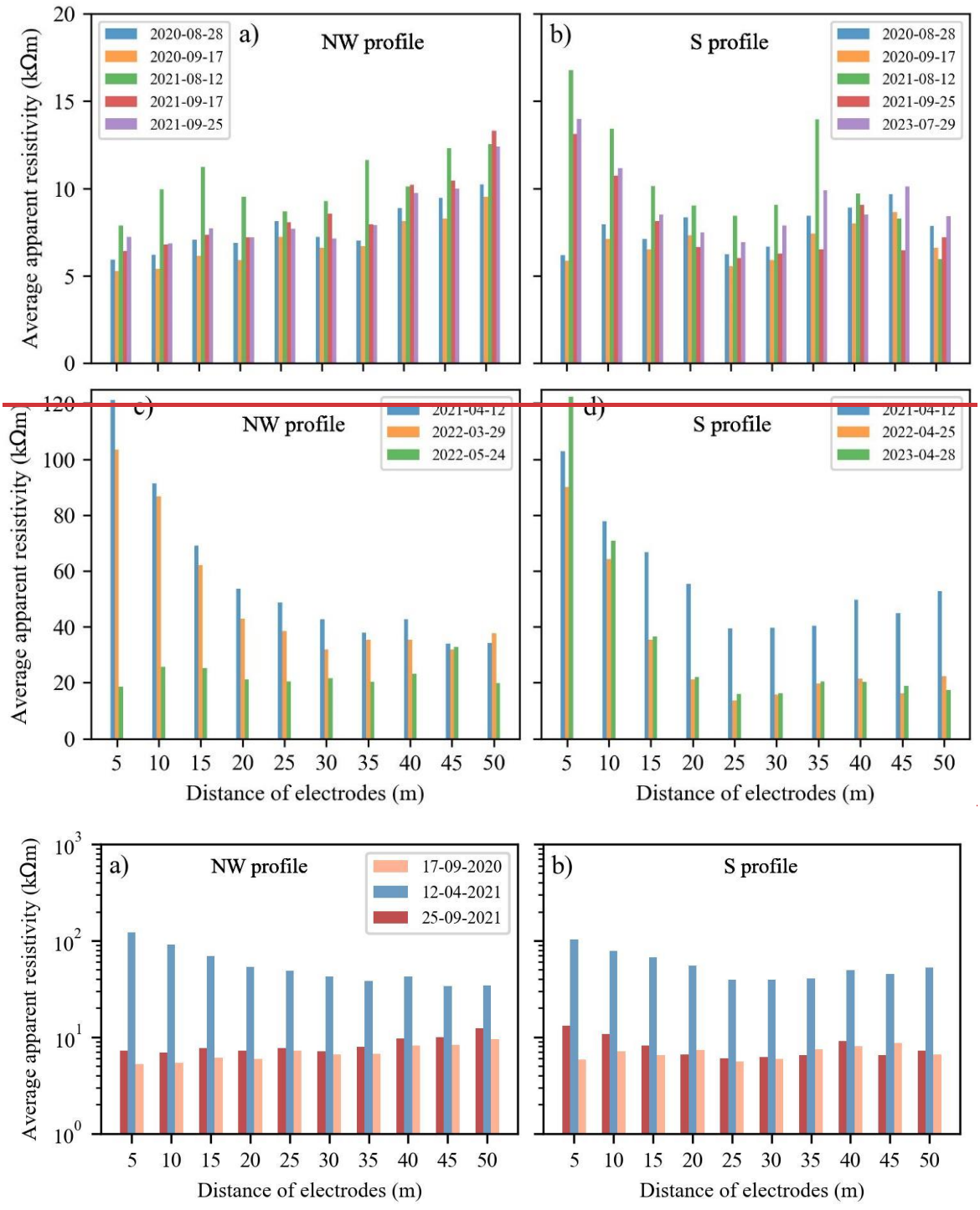

Figure 5~~5~~**.** Seasonal variations ~~Variations~~ of the average apparent resistivity at different electrode distances (*i.e.*, at varying depths of investigation). Data in spring show the same trend on both sides. In autumn, there is a divergence in the trend of average resistivities with depth on both sides, that is related to the hydrothermal conditions at each side. ~~The upper parts display data collected in summer and autumn (unfrozen condition at surface), and the lower parts show data collected in spring (frozen conditions at surface).~~

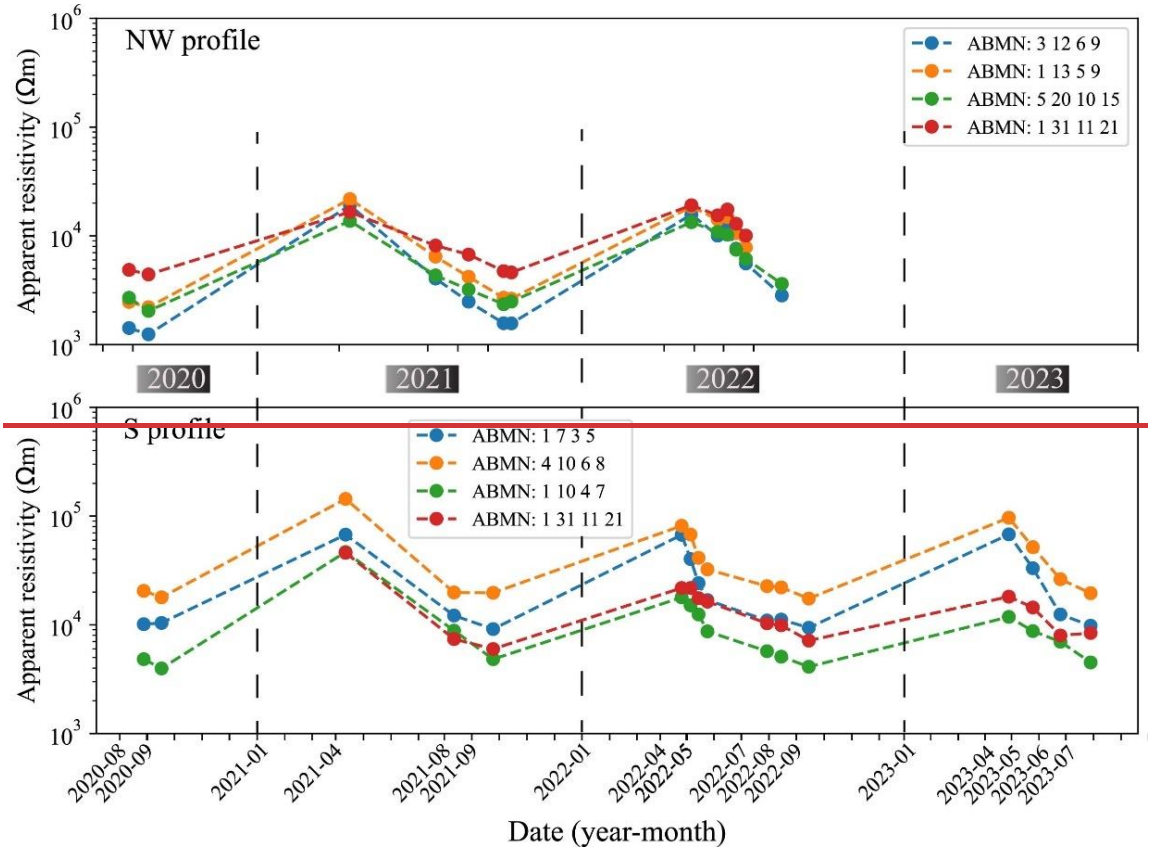

5.2. Internal structure of the site ~~Data inversion and interpretation~~

In order to have an overview of the internal structure of the study site based on the resistivity distribution, we carried out inversions of two long profiles (NW+S and NW+E). Figure 6~~7~~ shows the electrical resistivity tomogram from late summer 2020 (August 26th, 2020), where acquisition ~~at~~on both North-West and South sides (NW+S) was~~are~~ performed. The tomogram clearly reveals the site's internal structure, with low resistivity areas (warm-colored zones) indicating the relative positions of the infrastructure elements (elevator and galleries on both sides). It also shows the extent of the active layer (moderate resistivity areas near the surface), as well as the permafrost evidenced by high resistivity areas (represented in cool-colors). Although the lower part of the tomogram appears similar on both the NW and S profiles~~sides~~, which is expected since they lie in rockwalls that are alike regarding slope and aspect (the

lowest part of the S profile is deployed on the NWface as well, see Fig 1c), significant differences are evident in the upper part (*i.e.*, above the gallery level), revealing the contrast between sun-exposed (S side of fractured granite and exposed to strong insolation (Magnin et al., 2024) and shaded face (NW side of massive granite mostly dependent on the sensible atmospheric heat flux). The top part of the profile also reveals potential effects of strong lateral heat fluxes (Noetzli et al., 2007 ; Magnin et al., 2017) as the high-resistivity area is limited certainly due to the influence of the vicinity of the sun-exposed and warm face.~~For further analysis, the inverted resistivities were extracted from the four locations (P1 to P4) indicated by the red lines in Figure 7 and shown in the inset figure (see Fig. 7). In profile P1, a slight increase in resistivity is observed with depth, rising from 9.5 kΩm to 18 kΩm. Profile P2 exhibits significant variations with depth, characterized by an initial increase followed by a decrease, which can be attributed to the presence of permafrost between the active layer (close to the surface) and the effect of the elevator (at greater depths). Conversely, profile P3 shows higher resistivity near the surface (desaturation effect). The electrical resistivity decreases with depth, likely due to increased water saturation with depth in this area characterized by open fractures. Profile P4 shows a similar trend to profile P1 but exhibits a more pronounced gradient with depth (from 2 kΩm to 27 kΩm). This variation is attributed to heat transfer, particularly in areas close to the sun-exposed face.~~

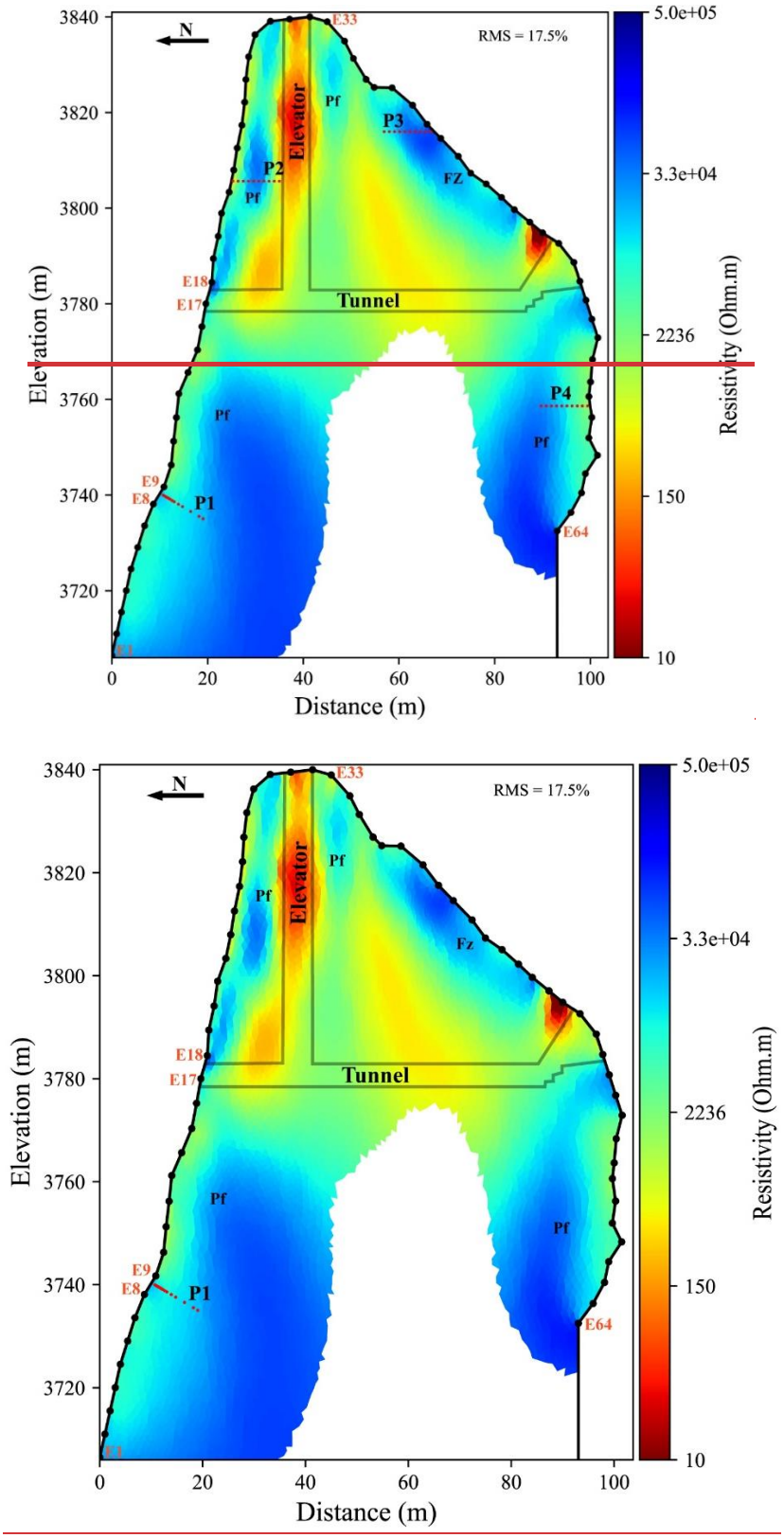

Figure 6~~7~~. Electrical resistivity tomogram over the NW+S profile measured on August 26, 2020. Grey lines indicate the approximative positions of infrastructure (galleries and elevator). Pf stands for Permafrost zone and Fz for Fractured Zone. E1 to E64 are Electrode numbers ~~are shown in red~~. Red dots at P1 ~~(P1 to P4)~~ indicate the positions of the thermal sensors in BH-NW. ~~extracted resistivity shown~~

~~in the inset figure. The insert shows the variation of resistivity with depth at the four locations (P1 to P4).~~

Figure ~~7~~8 provides an example of the resistivity tomogram for the combined NW and E profiles. This tomogram highlights the changes in resistivity associated with permafrost, active layer, and anthropogenic installation (such as the elevator and gallery (relatively far from the profile at the E side compared to S profile)). On the e~~E~~astern side, a thick active layer (> 5 m depth) is observed, with some r~~R~~esistive zones near~~close~~ the surface ~~and round th~~.~~e active layer can be seen, l ikely~~These resistive zones are likely fractured zones ~~resulting from water drainage at the end of the thawing season,~~ creating an unsaturated and air-filled zone, and ~~-~~surrounded by~~-~~ moderate ~~the active layer~~ resistivity regions where fractures are closed or where ~~no~~ drainage is~~or~~ weak or absent~~drainage could be existed.~~ ~~the active layer could be observed below a high resistivity layer that likely indicates the dry layer, and higher resistivity at depth that indicates the permafrost.~~ ~~Resistive zones close the surface and round the active layer can be seen, likely resulting from water drainage at the end of the thawing season, creating an unsaturated and air-filled zone surrounded by the active layer where no drainage or weak drainage could be existed.~~ D~~On the other hand, d~~ata acquisition on the Eastern side (E profile) encountered numerous challenges related to contact resistance, rockfalls and cable connections, resulting in long gaps and insufficient data for long time analysis or time-lapse inversion.

~~On the other hand, data acquisition on the Eastern side (E profile) encountered numerous challenges related to contact resistance, rockfalls and cable connections, resulting in long gaps and insufficient data for long time analysis or time-lapse inversion.~~ ~~After this overview of the internal structure, a time-lapse inversion of the data of each profile will be presented in the next section.~~

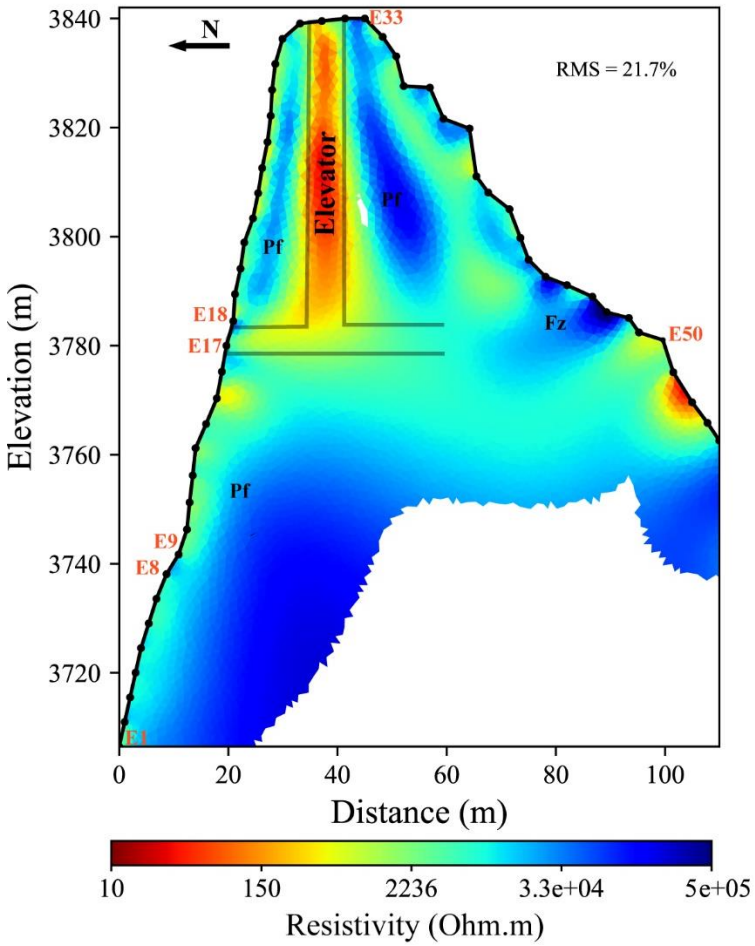

Figure ~~8~~7. Electrical resistivity tomogram over the profile NW+E at the end of summer (September 25, 2021). Data acquisition on the East profile run into problems related to electrodes contact and cable malfunction. The last 10 electrodes from the E profile were removed during processing due to connection issues. Pf stands for Permafrost zone and Fz for Fractured Zone.

5.3. ~~Time-lapse inversion~~Seasonal and interannual variations

In order to track the seasonal and interannual variations in the permafrost, ~~To track the resistivity changes associated with nonlinear heat transfer such as heat advection across the site,~~ a time-lapse inversion approach was employed to invert datasets for each profile (NW, S). The reference model was moved along with the inversion so that the difference to the preceding step is constrained. Figure ~~8~~9 shows the resistivity distribution~~results~~ after a~~of the~~ time-lapse

inversion of datasets from NW profile at different time intervals. Spatial and temporal changes in resistivity could be observed, while the anomaly related to the gallery (the warm-colored area (low resistivity area)) remains consistent over time. The permafrost identified by high resistivity, is observed in two zones, above and below the gallery. ~~As expected, the most significant variations in resistivity occur near the surface in the active layer where thawing and freezing are visible through the steady resistivity changes.~~ According to temperature analyzes conducted by Magnin et al. (2024), 2021 was cooler than both 2020 and 2022 (see Fig. 2). This is reflected in the tomograms by a more prominent permafrost (cool-colored zone ~~(more permafrost~~) in 2021 (Fig. 8~~9~~d~~e, f and g~~) in comparison with data in 2020 (Fig. 8b~~9c~~) ~~and 2022 (Fig. 9l, taking into account the difference in dates)~~. Furthermore, there is a significant variation in 2022 in the lower part of the tomograms (Fig. 8e ~~9l~~), possibly related to water infiltration in fractures that shortcut the heat transfer from the surface to depth (Hasler et al., 2011). ~~No evidence of water accumulation was observed from the geophysical measurements. It is suggested that the water table lies at lower altitude (Magnin and Josnin, 2021).~~ However, this area is uncertain, as it is located at the border ~~edge~~ of the tomogram where sensitivity is low. In addition, the RMS error is high in thi~~se~~ tomogram~~s~~, indicating high uncertainties. Therefore, this information should be carefully considered and verified with further measurements focused on the zone of interest. Unlike Offer et al. (2025), ~~N~~no evidence of water accumulation was observed from the geophysical measurements on the NW face. It is suggested that the water table lies at lower altitude (Magnin and Josnin, 2021).

Instead of analyzing temporal resistivity changes in absolute terms, Figure 8~~re 10~~ (f - i) illustrates the resistivity variation ratio between two subsequent measurements. This approach facilitates the tracking and visualization of small changes in resistivity. A value of 1 (represented in white color) corresponds to no change in resistivity between the two measurements (reflecting consistent geological conditions, topographic effects, infrastructure

or no considerable change in temperature over time), while the blue color indicates that the resistivity increased over time, and the red color represents the inverse. It can be observed that, the seasonal variations are more pronounced as illustrated in Figure 8g, h and i. The effects of freezing-thawing are marked by the maximum variations close to surface, in the active layer. In contrast, at short time interval (few weeks), only minor variations are noted (*e.g.*, Fig. 8f). Figure 8i, a decrease in resistivity near the surface at about 3780 m, could be related to water flow around the gallery where water infiltration is observed by local staff every summer (personal communication) sush as a specific water diversion system was installed to protect tourists from water flows.

Extended times lapse inversion of datasets from NW and S face are presented in appendix C.

~~It can be observed that at short time interval (few days to weeks), the variation in resistivity is negligible (*e.g.*, Fig. 10b, e, f and j). At longer time interval (few weeks to months), only minor variations are noted (*e.g.*, Fig. 10a, h and i), while the seasonal variations are more pronounced as illustrated in Figure 10c, d and g. The effect of freezing is evident, marked by an increase in resistivity of the active layer (Fig. 10c and g). In contrast, Fig. 10d shows the maximum decrease in resistivity near the surface, as expected due to the thawing in the active layer. Further observations on Figures 10a, b and e indicate a local increase in resistivity, as shown by the blue color zone between 3780 and 3800 m a.s.l. That could be associated with water desaturation and drainage observed in the gallery just below this zone.~~

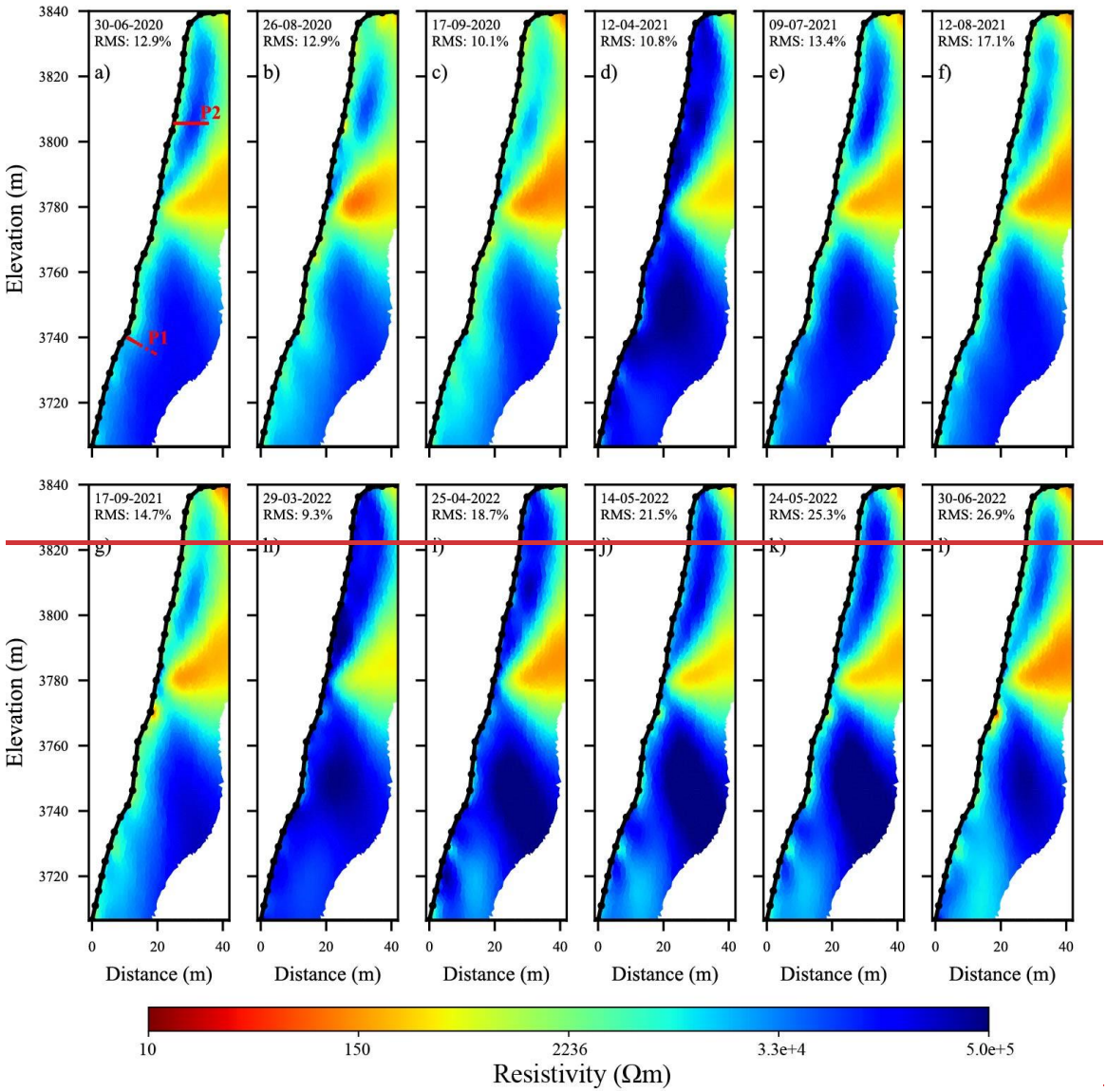
30-06-2020
RMS: 12.9%
a)
26-08-2020
RMS: 12.9%
b)
17-09-2020
RMS: 10.1%
c)
12-04-2021
RMS: 10.8%
d)
09-07-2021
RMS: 13.4%
e)
12-08-2021
RMS: 17.1%
f)
P1
P2
17-09-2021
RMS: 14.7%
g)
29-03-2022
RMS: 9.3%
h)
25-04-2022
RMS: 18.7%
i)
14-05-2022
RMS: 21.5%
j)
24-05-2022
RMS: 25.3%
k)
30-06-2022
RMS: 26.9%
l)
Elevation (m)
3840
3820
3800
3780
3760
3740
3720
0
20
40
Distance (m)
10
150
2236
3.3e+4
5.0e+5
Resistivity (Ωm)

563

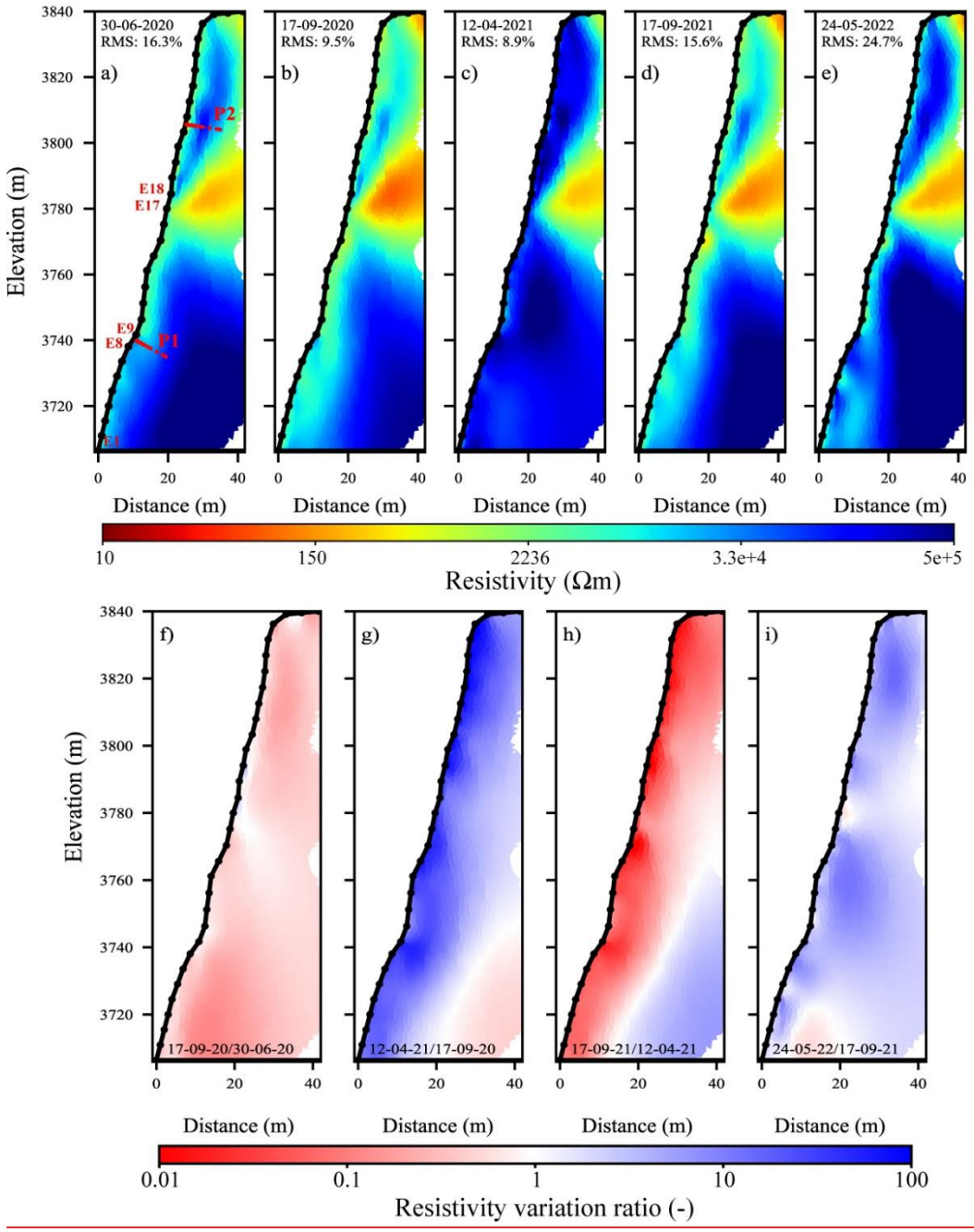

Figure ~~9~~8. Seasonal and interannual variations of electrical resistivity at NW side. Upper part) ~~E~~electrical resistivity tomograms at different dates (from June-2020 to June-2022) ~~along the NW side (NW profile)~~. The conductive zone (in warm colors) denotes the presence of the gallery and elevator (see Fig. 6~~1c~~). The red dots (P1 in panel a) indicate the positions of the thermal sensors in the borehole BH-NW. Data presented on Figures 9~~13~~, ~~14~~10 and 1~~5~~1 are extracted at the red dots (P1 and P2). Lower part) r~~ and P2).~~

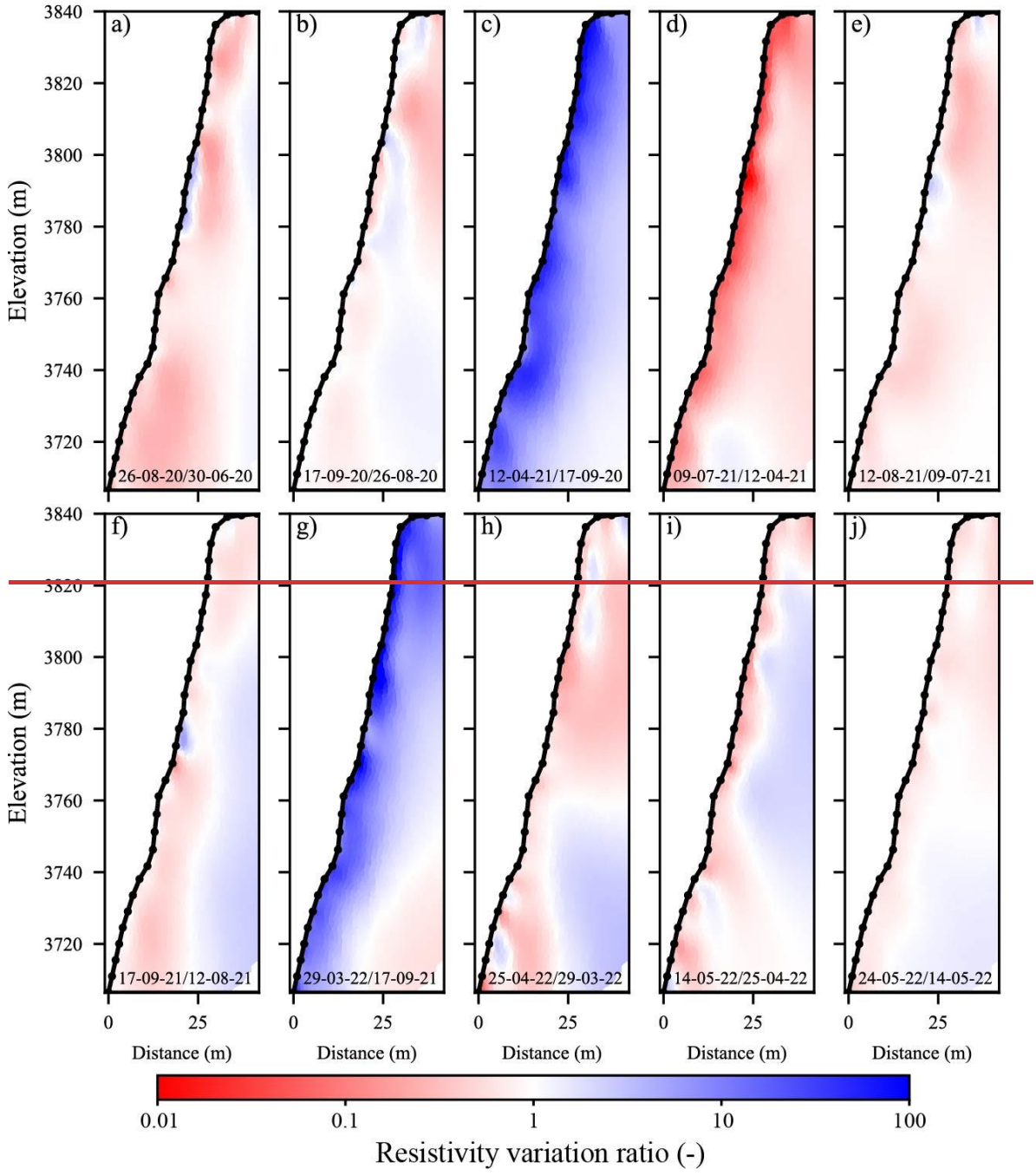

~~Figure 10.~~ ~~R~~esistivity variation ratio between consecutive electrical resistivity tomograms ~~(shown in Fig. 9) along the NW side~~. Blue colors indicate an increase in resistivity, while red colors represent a decrease in resistivity from one measurement to the next.

Inverted resistivities at P1 (BH-NW) and a virtual borehole at P2 (see Fig. 8) are presented in Figure 9. The extracted resistivities show that the variation of resistivity with depth is more

pronounced at P2. This higher variation could indicate a higher water content in the active layer at P2 compared to P1 (higher temperature), and thicker active layer at P2. The presence of the elevator contributes to heat the granite from inside decreasing the resistivity above the tunnel in P2. The greater thickness of AL in the upper section can be explained by the 3D heat transfer and the proximity of the shaded face (NW side) to the sun-exposed faces (S side) in the top part. In the lower section (profile P1), the contrast between the resistivity in the active layer and that in the permafrost is not significant, which may be due to low water content where the porosity is around 1 %, or due to high surface conductivity in granite. However, it is important to note that the ALT is about 2.7 m at the end of summer (from BH-NW measurements, see Fig. A1), and the smallest quadrupole spacing is 15 m, which is insufficient to capture thin variations close to surface (Edwards, 1977). We could notice a slight decreases of resistivity over time in the permafrost (between 30-06-2020 and 30-06-2022). Furthermore, in 2021, resistivity values were higher in both the upper and lower parts compared to 2020 and 2022, and this is aligned with temperature measurements (see Fig. 2, or details in Magnin et al. (2024)).

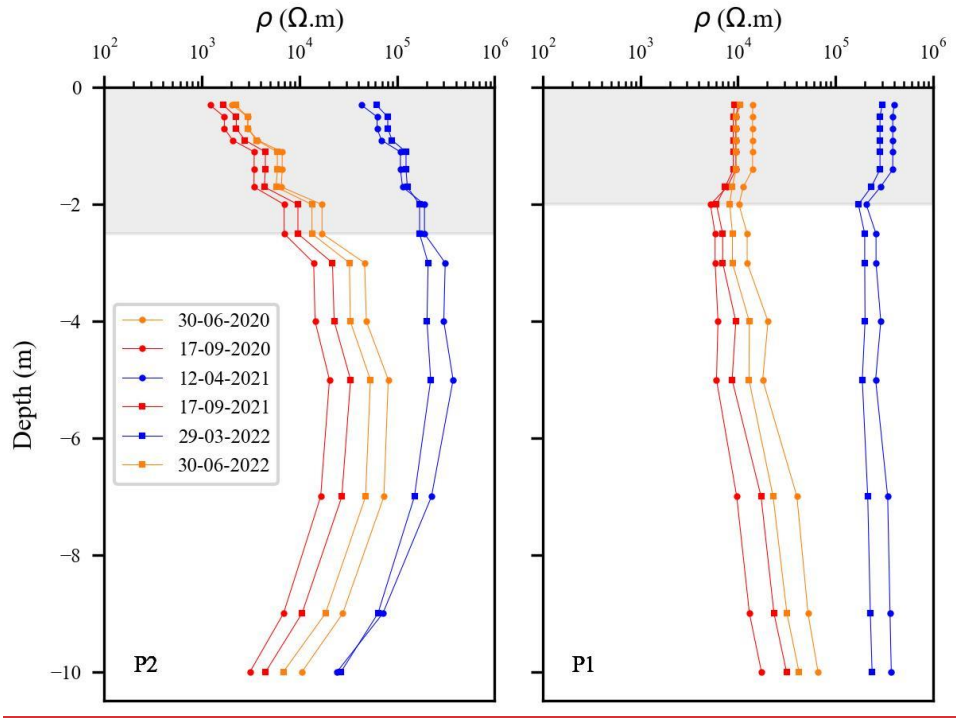

598 **Figure 9.** Resistivity extracted over depths at different dates and locations (P1, P2). Resistivities
599 extracted from tomograms in Fig. D1.
600

601 ## 5.4. Temperature - resistivity relationship

602 Extracted resistivity at P1 is superimposed at borehole BH-NW, where temperature
603 measurements are available. We use these two datasets (*i.e.*, temperature and resistivity
604 measurements at the same location, BH-NW) to explore the potential for estimating temperature
605 based on the electrical resistivity measurements and for a quantitative evaluation of the T-R
606 relationship determined in a laboratory.

607 It is known that, when temperature > 0 °C (*i.e.*, the case in the active layer), resistivity
608 depends on multiple variables, including porosity, water content, water salinity, Cation
609 Exchange Capacity (CEC) and temperature (Revil et al., 2018) and will be difficult to model or
610 to predict the resistivity value at the active layer. In contrast, under frozen conditions, resistivity
611 of a medium is primarily controlled by the remaining unfrozen pore water content, and is
612 assumed to be dependent on temperature, while the other parameters remain constant.
613 Therefore, the extracted resistivities in the frozen zone were converted to temperature using the
614 petrophysical model in Equation 2 (Duvillard et al., 2021; 2018; Coperey et al., 2019). Figure
615 10 shows the measured temperature alongside the estimated temperature from ERT data, plotted
616 against depth at different dates (in summer and autumn). A good agreement can be observed
617 between the measured and estimated temperature in frozen conditions, with differences of less
618 than ±1 °C at depths between 4 and 10 m. This suggests that temperature distribution across the
619 site can be calculated using this model (e.g., Duvillard et al., 2021), assuming the medium is
620 homogenous and resistivity variations are solely attributed to temperature. However, at AdM,
621 this condition is not satisfied due to the infrastructure, which creates a conductive zone within
622 the medium (see Figs. 6, 7). In the active layer, predicting temperature is not feasible since
623 temperature is not dominant factor affecting resistivity. The data collected under frozen

condition at the surface (*i.e.*, measured in winter and spring with high contact resistance) resulted in large discrepancy between the estimated and measured temperature, and could not be used to estimate temperature. A-ERT measurements still a challenge in frozen condition at surface.

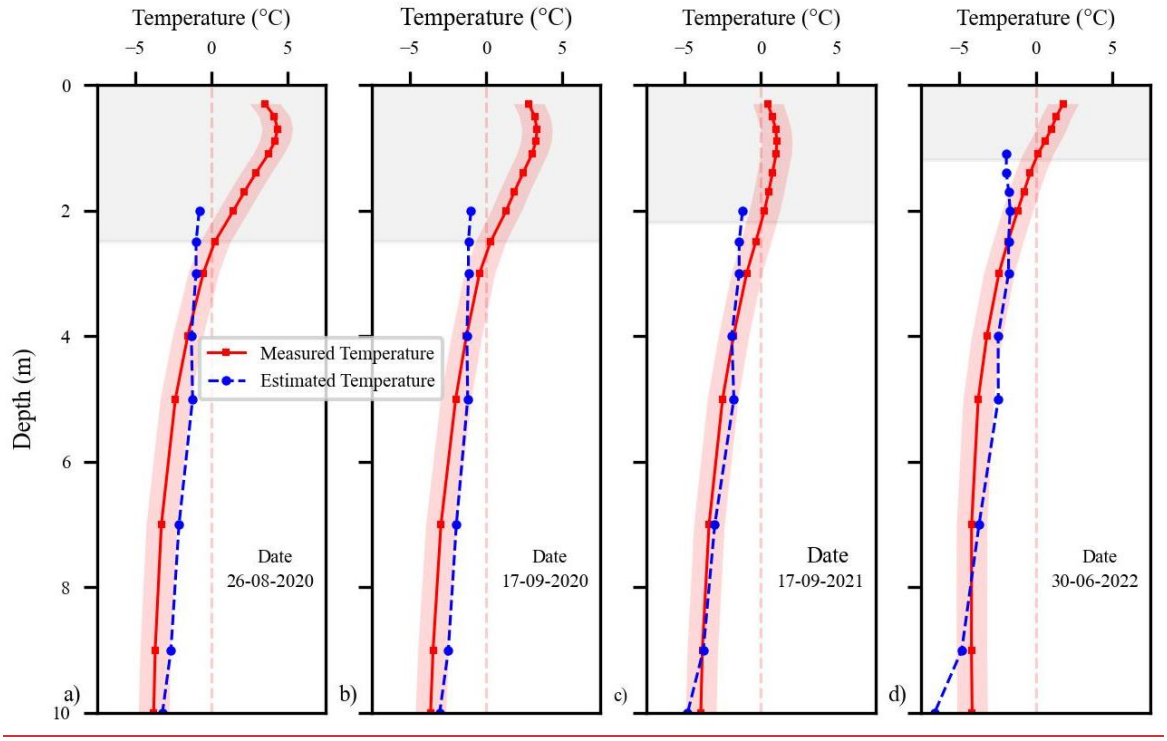

Figure 10. Comparison between measured temperatures in BH-NW and estimated temperatures derived from geophysical measurements (*i.e.*, extracted resistivity values at different dates) using the petrophysical model in Equation 2. The gray-shaded area indicates the extent of the active layer at the time of measurement. The red-shaded zones show the ±1 °C range around the measured temperature.

To go further in our analysis, Figure 11 shows the extracted resistivity at P1 vs. temperature data measured in BH-NW at different dates. Laboratory measurements on both granite samples (labeled Sample AdM and Sample Cosmiques) are also shown. Three key observations can be made: first, data collected in winter and spring (frozen conditions at surface), presented by blue symbols, show resistivity values higher than those expected based on laboratory measurements, which aligns with the field observations reported by Maierhofer

et al (2024). This could be related to the salt segregation during freezing, which may enhance conductivity of pore water and, consequently reduce resistivity of samples. Second, at higher temperature (unfrozen conditions at surface), a linear trend is observed that aligns with laboratory measurements for part of datasets. The difference in resistivity between field and laboratory data under unfrozen conditions may be attributed to the heterogeneity at the field scale and/or the difference in water content and water salinity between laboratory and field environments. The laboratory measurements were conducted in saturated conditions (saturation was performed under vacuum using degassed water). Third, the field data exhibit greater dispersion compared to laboratory data, which can be attributed to several factors, including 3D effects at the site, the influence of infrastructure and heterogeneity at different scales (from fractures scale to pore scale). In addition, there is a difference in resolution between the two field measurements: temperature measurements are local, while resistivity measurements account for a larger volume.

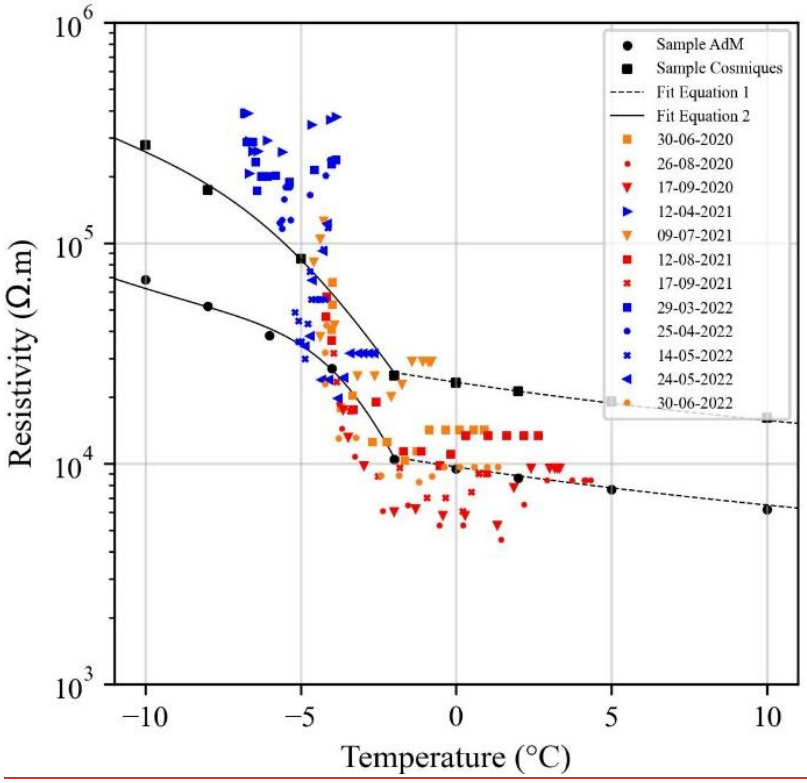

Figure 11. Resistivity vs. temperature. Resistivity is extracted from the tomograms in Figure 9 at location P1. Temperature is measured by sensors at BH-NW. Laboratory data on two granite samples and fitting with Equation 1 and 2 are shown too.

5.5. Hydrogeological dynamics

~~On the south side, time-lapse inversion was also conducted using the same inversion parameters as those used on the NW side (Fig. 9). Figure 11 presents the results of the time-lapse inversion of datasets from S profile at various time intervals. Two phenomena can be distinguished on this side: first, in the lower part (*i.e.*, below the gallery denoted by the warm-colored area), seasonal variations in permafrost are clearly observed and could be tracked over time. In Figures 11a, c, d, g, h and l (measurements taken in summer and autumn), the steady thawing of active layer through heat conduction from the surface is evident in the lower part. Second, in the upper part of the profile (*i.e.*, above the gallery), the seasonal variations are less pronounced in this fractured area. This region is characterized by strong insolation (*i.e.*, sun-exposed area) that dries the rock and fractures, where drainage of water (of melted ice) reduces water saturation, thereby increasing resistivity near the surface as a result of air-filled pores and fractures. The water infiltration and drainage in this area increase the thickness of the active layer (*e.g.*, Figure 11a, d, g and h), and create a conductive zone observed beneath the fractured area where drainage is minimal or nonexistent (*e.g.*, Fig 11a, c, d and h).~~

~~Figure 12 illustrates the resistivity variation ratio between successive measurements on the S profile. The dynamics of the active layer are evident, with freezing-thawing effects visible near the surface (*e.g.*, Fig. 12a, d, and g). The heat effect (*i.e.*, decrease in resistivity values near the surface) is more pronounced in the lower section (below the gallery). Another type of anomaly could be observed at greater depth, where heat and/or cool waves resulting of heat~~

~~transfer (with delay) lead to local variations at greater depth (*e.g.*, Fig. 12d, e, g and i). In contrast, the fractured zone in the upper portion obscures the temperature dependency of resistivity due to fluctuations in air and water content (*i.e.*, resistivity in this zone is impacted by factors beyond just temperature). Water infiltration in this area could explain the rapid and significant decrease in resistivity observed between 3790 and 3820 m a.s.l. (*e.g.*, Fig. 12c, f, and j), which increases the thickness of active layer in this zone.~~

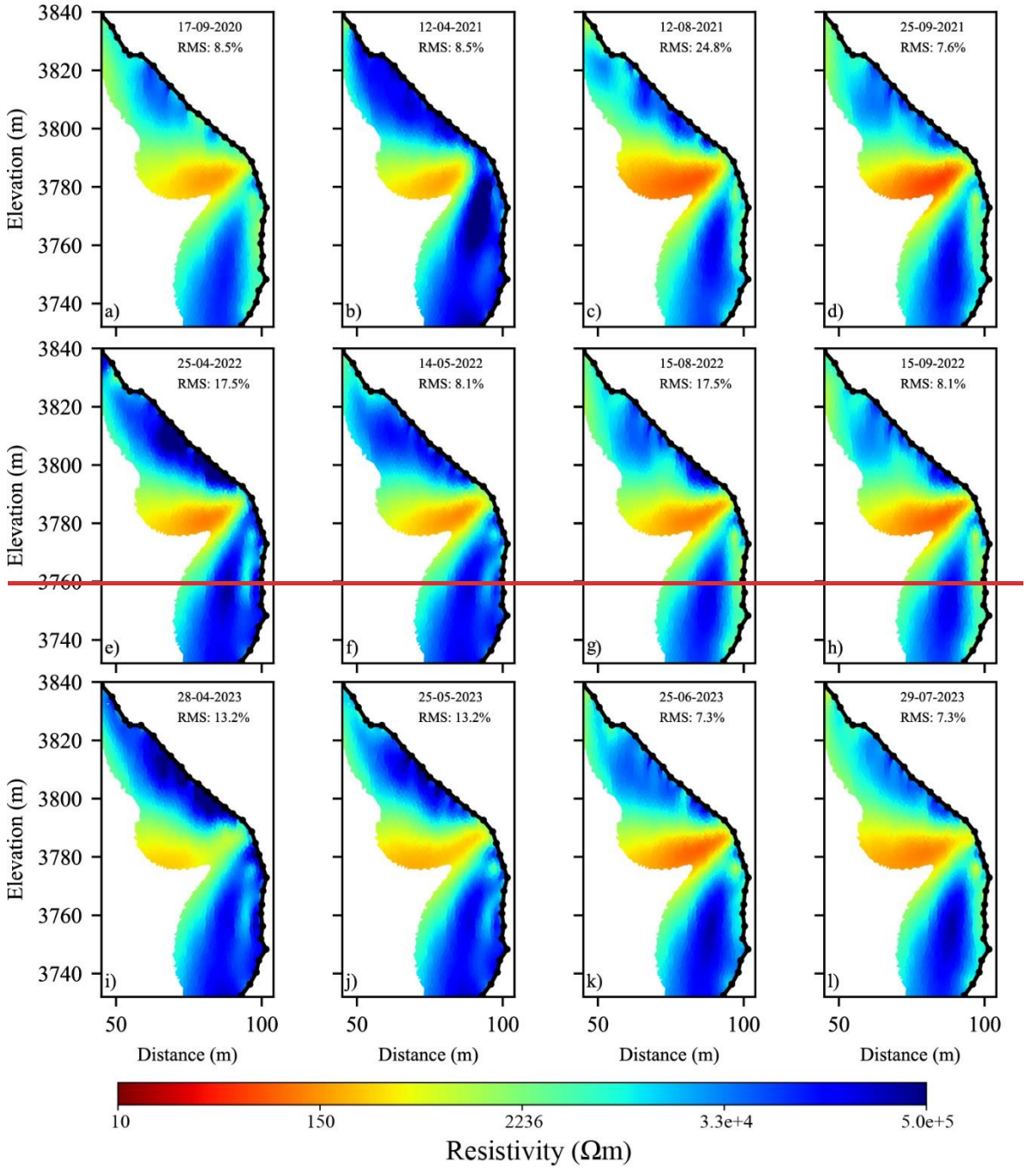

~~**Figure 11.** Electrical resistivity tomograms at different dates (from September 2020 to July 2023) along the South side (S profile). The conductive zone (in warm colors) explained by the presence of the gallery (see Fig. 1d). Red arrows show the positions of possible infiltration or drainage. Data presented on Figure 13 are extracted at the red dots (P3 and P4) in panel a.~~

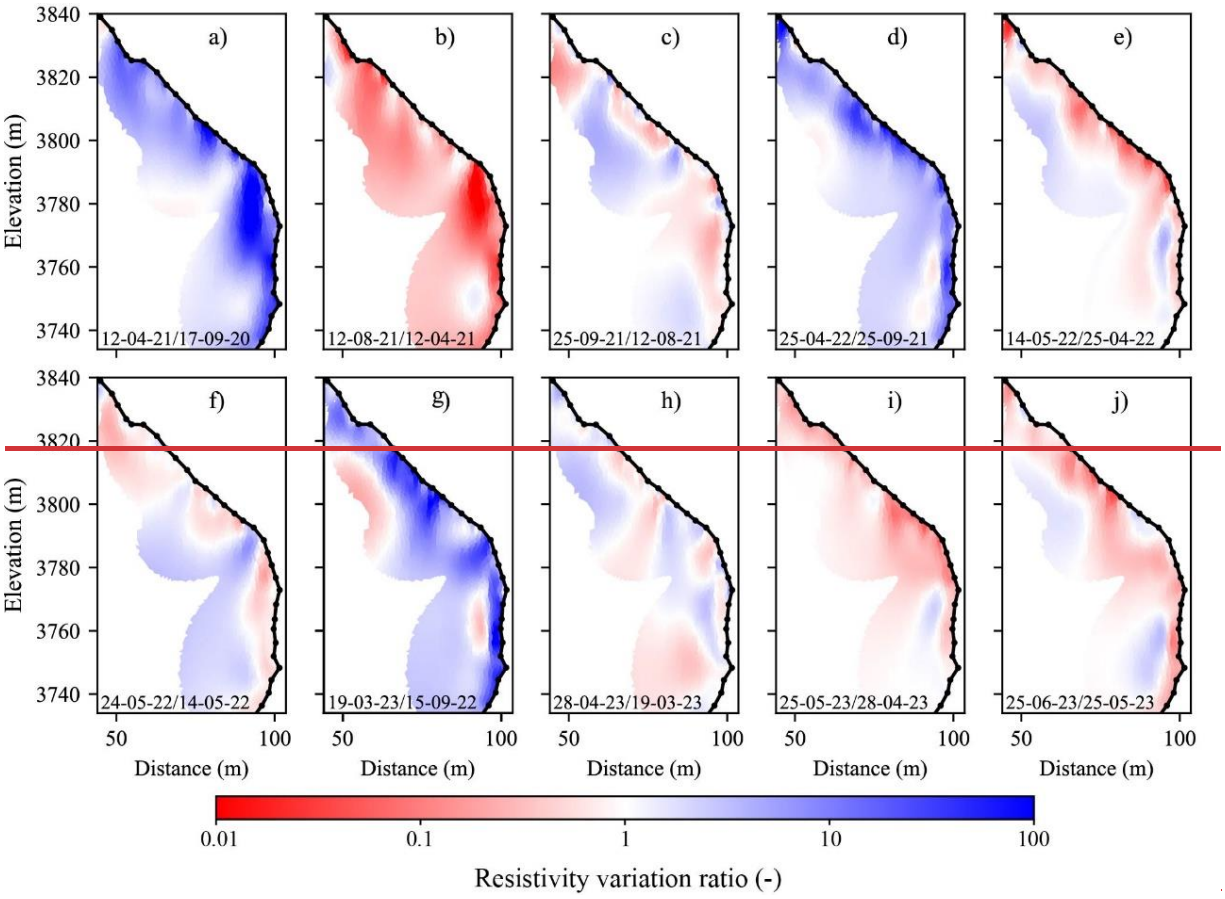

~~**Figure 12.** Resistivity variation ratio between consecutive electrical resistivity tomograms (shown in Fig. 11) along the South side. Blue colors indicate an increase in resistivity, while red colors represent a decrease in resistivity from one measurement to the next.~~

One of the objectives of this study was to assess the hydrogeological dynamics. While we could not precisely identify the infiltration and drainage pathways or the water table (which may be at a lower altitude) using ERT measurements, we observed several instances that could be classified as evidence of water flux. Due to gaps in the data and the high CR, which affect data quality and reduce the number of points in datasets (because of disconnected electrodes), the analysis of the time series did not yield meaningful information. That is why we used

selected datasets and we compared results of times-lapse to get information about the water infiltration and drainage.

On the south side, time-lapse inversion was also conducted using the same inversion parameters as those used on the NW side (Fig. 8 and D1). Figure 12 presents the results of the time-lapse inversion of datasets from S profile at various time intervals. In the upper part of the profile (*i.e.*, above the gallery), the seasonal variations are less pronounced in this fractured area. This region is characterized by strong insolation (*i.e.*, sun-exposed area) that dries the rock and fractures, where drainage of water (of melted ice) reduces water saturation, thereby increasing resistivity near the surface as a result of air-filled pores and fractures. The water infiltration and drainage in this area increase the thickness of the active layer (*e.g.*, Figure 12a, d, g and h), and create a conductive zone observed beneath the fractured area where drainage is minimal or nonexistent (*e.g.*, Fig 12a, c, d and h), compared to other tomograms with resistive zone (*e.g.*, Fig 12b, e and). The decrease in resistivity in this zone could be interpreted as a result higher water saturation caused by the circulation of snowmelt or rainfall water. The absence of precipitation data at the site prevented the correlation and validation of the ERT observations with rainfall events.

With the AdM setting, we can also hypothesize that the saturated conditions are almost never reached. There is water circulation but no accumulation of water and/or water column development because the water table is likely lower than the area covered by the measurements (Magnin and Josnin, 2021), conversely to Offer et al. (2025) at the Kitzsteinhorn for example. Indeed, our investigation is in a different setting: high altitude peak lying ~2000 m above the water table (Magnin and Josnin, 2021) while in the Kitzsteinhorn outcrops from a glaciated areas with a probably much closer water table.

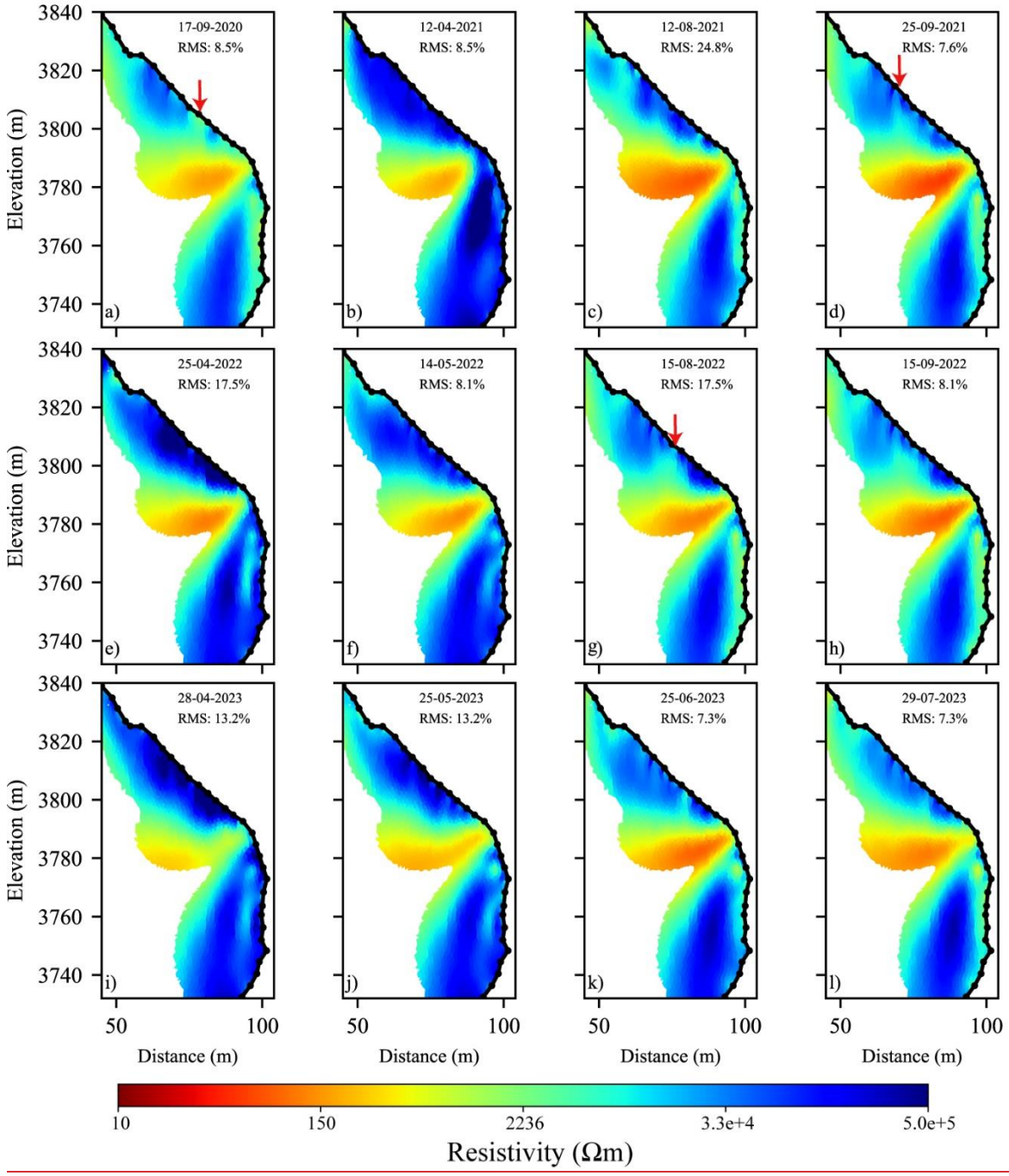

Figure 12. Electrical resistivity tomograms at different dates (from September-2020 to July-2023) along the South side (S profile). The conductive zone (in warm-colors) explained by the presence of the gallery (see Fig. 6).

6. Discussion

In this study, we u~~se~~tilize repeated and ~~A~~automated ~~-~~ERT to investigate the evolution of permafrost at a high mountain site. As expected, data from A-ERT are of lower quality compared to manual measurements, where the operator can intervene to improve contact

resistance after each electrode check (Doetsch et al., 2015; Hilbich et al., 2009). The high contact resistance is the main problem for getting good and durable A-ERT. Conducting ERT in frozen surface conditions on rockwall permafrost remains challenging because of the high contact resistance. Various approaches were tested to improve CR. For instance, duplicated electrodes provided a durable and significant improvement in RC (~ one order of magnitude reduction in CR), helping to enhance data quality.

Time lapse inversion of the measured resistivity showed the seasonal and interannual variations (Fig. 8 and 9). We observe that resistivity decreased over time at greater depths (*e.g.*, at P1 and P2, comparing data from July 30, 2020 and July 30, 2022), indicating degradation of the permafrost such as also revealed by borehole measurements (Magnin et al., 2024). However, this decrease in resistivity is minor, likely due to the relatively short observation period of two years at NW side and 4 years at S side. A thicker active layer is observed at the upper section, which can be attributed to three-dimensional heat transfer processes and the close proximity of the shaded north-west face to the sun-exposed southern faces in the upper part of the slope (Noetzli et al., 2007). The presence of the galleries and elevator contributes also to heat the granitic peak from inside decreasing the resistivity above the tunnel.

The contrast between the resistivity in the active layer and that in permafrost is not significant (in the lower section on the NW side (P1 Fig. 9)), which may be due to low ice content/water content where the porosity is around 1 %, or due to high surface conductivity in granite. The alteration of granite involves the transformation of primary minerals (mica and alkali feldspars) into secondary clay minerals (such as kaolinite), which are known for their high cation exchange capacity and, consequently, their contribution to surface conductivity (Piolat et al., 2025; Revil et al., 2024). Additionally, the sensitivity of the used dispositive (with a smallest quadrupole length of 15 m) could affect the resolution of ERT image near the surface (Binley and Kemna, 2005).

We take advantage of the existing temperature borehole (BH-NW) located on the NW face along the geophysical profile (NW profile) to validate our interpretation and temperature estimations. For further analyses, inverted resistivity values are extracted at the borehole location (P1) for all temperature sensor depths up to 10 m (see Fig. 9), as well as at three other locations (P2, P3 and P4) illustrated in Figures 9 and 11.

6.1. Permafrost dynamics from seasonal to pluri-annual time scale

The dynamics of the Active Layer (AL) are generally illustrated by the seasonal variations shown in Figures 9 and 11. The tomograms show the overall trend and the distribution of active layer and permafrost in the area. Data extracted at different locations, above and below the gallery (P1, P2 in Fig. 9 and P3, P4 in Fig. 11), are presented in Figure 13. These extracted resistivities reveal that the active layer is thicker in the upper section compared to the lower part, and that resistivity decreases over time in the permafrost.

On the NW side (P1 and P2), the variation of resistivity with depth is more pronounced at P2, which indicates a thicker AL compared to P1. The greater thickness of AL in the upper section can be explained by the 3D heat transfer and the proximity of the shaded face (NW side) to the sun-exposed faces (S side) in the top part (Noetzli et al., 2007). In the lower section at NW side (P1 in Fig. 13), the contrast between the resistivity in the active layer and that in the permafrost (frozen zone) is not significant, which may be due to low ice content where the porosity is around 1 %, or due to high surface conductivity in granite. The alteration of granite involves the transformation of primary minerals (mica and alkali feldspars) into secondary clay minerals (such as kaolinite), which are known for their high cation exchange capacity and, consequently, their contribution to surface conductivity (Piolat et al., 2025; Revil et al., 2024). However, it is important to note that the smallest quadrupole spacing is 15 m, which is insufficient to capture thin variations close to surface (Binley and Kemna, 2005).

On the South side (the sun-exposed face), above the gallery lies the fractured zone. The extracted resistivities at P3 (Fig. 13) reveal higher values compared to the NW side (P2), showing a difference of more than one orders of magnitude at the same altitude and time. The resistivity along P3 decreases slightly with depth, indicating that almost the entirety of P3 is within the active layer. In this zone, the active layer is thicker due to the fractures, which facilitate the heat transfer and water flow. Below the gallery at P4 (Fig. 13), the active layer is more distinct compared to P1 on the NW side, displaying more pronounced variations in resistivity with depth. Below the gallery on both sides, we observe that resistivity decreased over time at greater depths (e.g., at P1, comparing data from July 30, 2020 and July 30, 2022, and at P4, comparing data from April 12, 2021 and April 28, 2023), indicating degradation of the permafrost. However, this decrease in resistivity is minor because the observation period is short.

~~Furthermore, in 2021, resistivity values were higher in both the upper and lower parts compared to 2020 and 2022, and this is aligned with temperature measurements (see Fig. 2) (see details in Magnin et al. (2024)). This indicate that A-ERT is able to reveal consistent permafrost evolution.~~

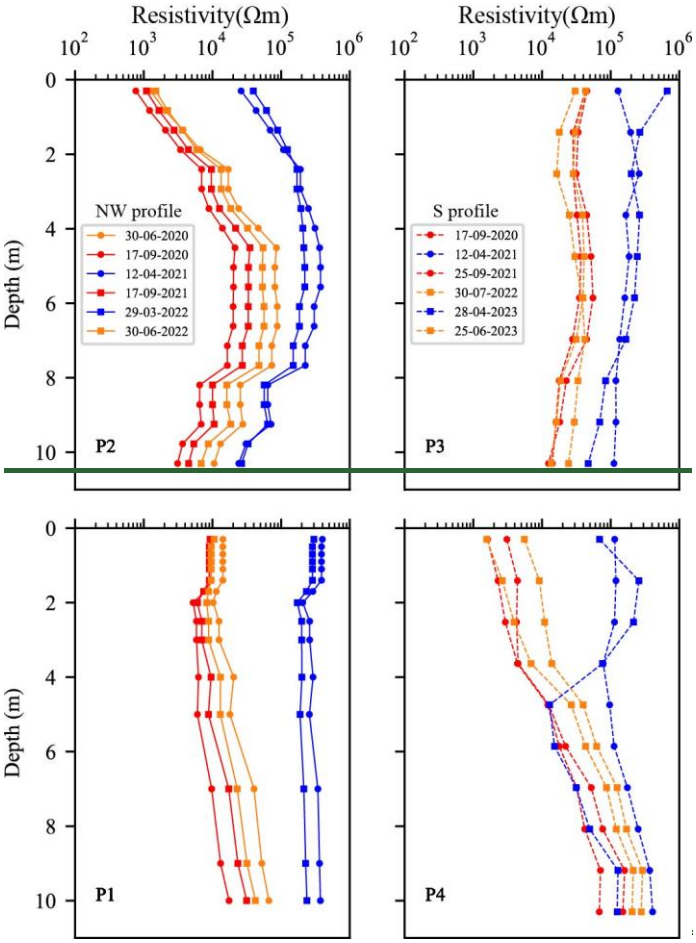

~~Figure 13. Resistivity extracted over depths at different locations. Resistivity extracted from tomograms on Figure 9 at P1 and P2, and from tomograms on Figure 11 at P3 and P4.~~

~~6.2. Temperature - resistivity relationship~~

~~Extracted resistivity at P1 is superimposed at borehole BH-NW, where temperature measurements are available. We use these two datasets (i.e., temperature and resistivity measurements at the same location, BH-NW) to explore the potential for estimating temperature based on the electrical resistivity measurements.~~

~~It is known that, when temperature > 0 °C (i.e., the case in the active layer), resistivity depends on multiple variables, including porosity, water content, water salinity, Cation Exchange Capacity (CEC) and temperature (Revil et al., 2018) and will be difficult to model or to predict the resistivity value at this stage. In contrast, under frozen conditions, resistivity is assumed to be primarily dependent on temperature, while the other parameters remain constant. Therefore, the extracted resistivity was converted to temperature using the petrophysical model in Equation 2 (Duvillard et al., 2021; 2018; Coperey et al., 2019) in the frozen zone. Figure 14 shows the measured temperature alongside the estimated temperature~~

from ERT data, plotted against depth at different dates (in summer and autumn). A good agreement can be observed between the measured and estimated temperature in frozen conditions, with differences of less than 1 °C at depths between 4 and 10 m. The data collected under frozen condition at the surface (i.e., measured in winter and spring with high contact resistance) resulted in large discrepancy between the estimated and measured temperature, and could not be used to estimate temperature.

The estimated temperature presented in Figures 14 indicate that the proposed model (Equation 2) can accurately reproduce the temperature. Here we used data extracted after time-lapse inversion, however, conducting individual inversion and adjusting the inversion parameters can enhance this estimation of temperature. This suggests that temperature distribution across the site can be evaluated using this model (e.g., Duvillard et al., 2021), assuming the medium is homogenous and resistivity variations are solely attributed to temperature. However, at AdM, this condition is not satisfied due to the infrastructure, which creates a conductive zone within the medium (see Figs. 7, 9 and 11).

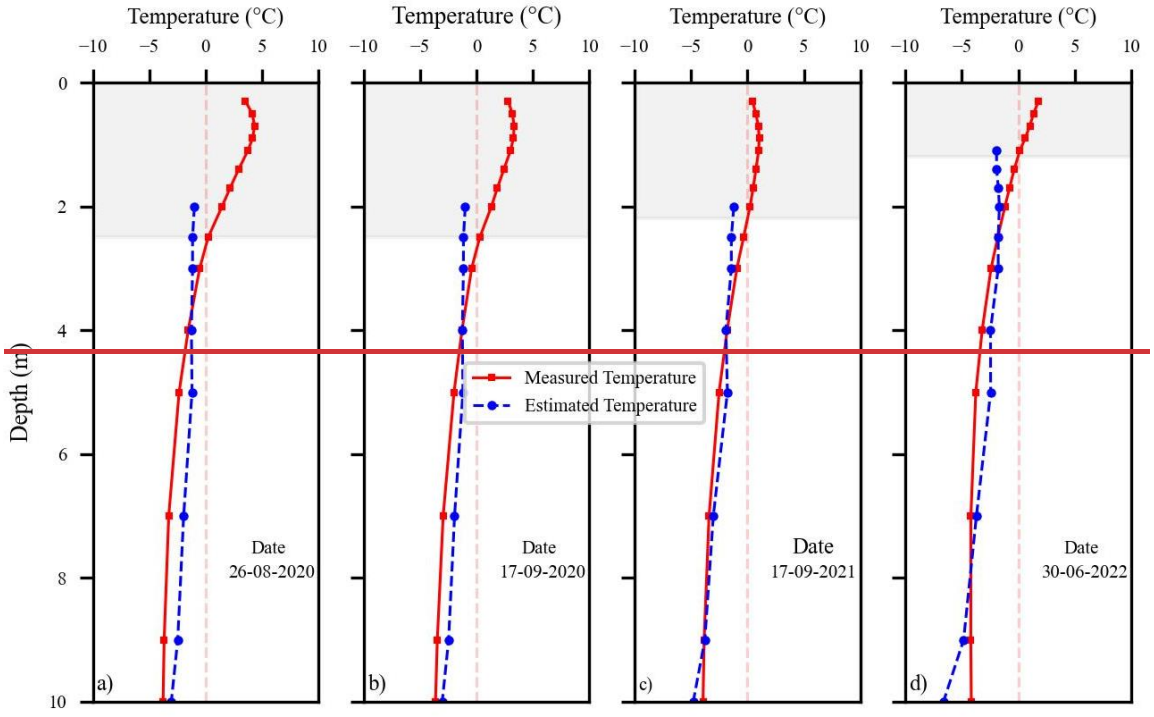

Figure 14. Comparison between measured temperatures in BH-NW and estimated temperatures from geophysical measurements (i.e., extracted resistivity values at different dates) using the petrophysical model in Equation 2. The gray-shaded area marks the extent of the active layer at the time of measurement. There is good agreement between measured and estimated temperature, with differences of less than 1 °C at depths 4 to 10m. In the active layer, predicting temperature is not feasible since temperature is not dominant factor affecting resistivity.

~~To go further in our analysis, Figure 15 shows the extracted resistivity at P1 vs. temperature data measured in BH-NW at different dates. Laboratory measurements on both granite samples (labeled Sample AdM and Sample Cosmiques) are also shown. Two key observations can be made: first, data measured in winter and spring (frozen conditions at surface) indicated by blue symbols, resistivity values are higher than what would be expected based on the laboratory measurements, in agreement with the field observations in Maierhofer et al (2024).~~

~~Second, at higher temperature (i.e., unfrozen conditions at surface), a linear trend is observed aligning with laboratory measurements for part of datasets. The difference of resistivity between field data and laboratory data in unfrozen conditions may be attributed to difference in water content and water salinity between field and laboratory conditions. The laboratory measurements were conducted in saturated conditions (saturation was performed under vacuum using degassed water). The freezing point, which is expected to result in a significant change in resistivity (as observed in laboratory measurements), does not exhibit the same effect in field. Actually, the transition between frozen and unfrozen conditions is not clearly distinguished in field. However, some datasets show gradual increase in resistivity when temperature decreased. Therefore, we hypothesize that the freezing occurs gradually at temperatures ranging between -0.5 and -2.5 °C. This point needs to be addressed in further research with smaller dispositive to improve the resolution of geophysical measurements.~~

~~This lack of clarity, observed between field data and laboratory data, may be attributed to several factors, including 3D effects at the site, the influence of infrastructure and heterogeneity at different scales (from fractures scale to pore scale where varying pore sizes led to variable residual water content available for electrical conduction). In addition, there is a difference in resolution between the two measurements: temperature measurements are local, while resistivity measurements account for a larger volume.~~

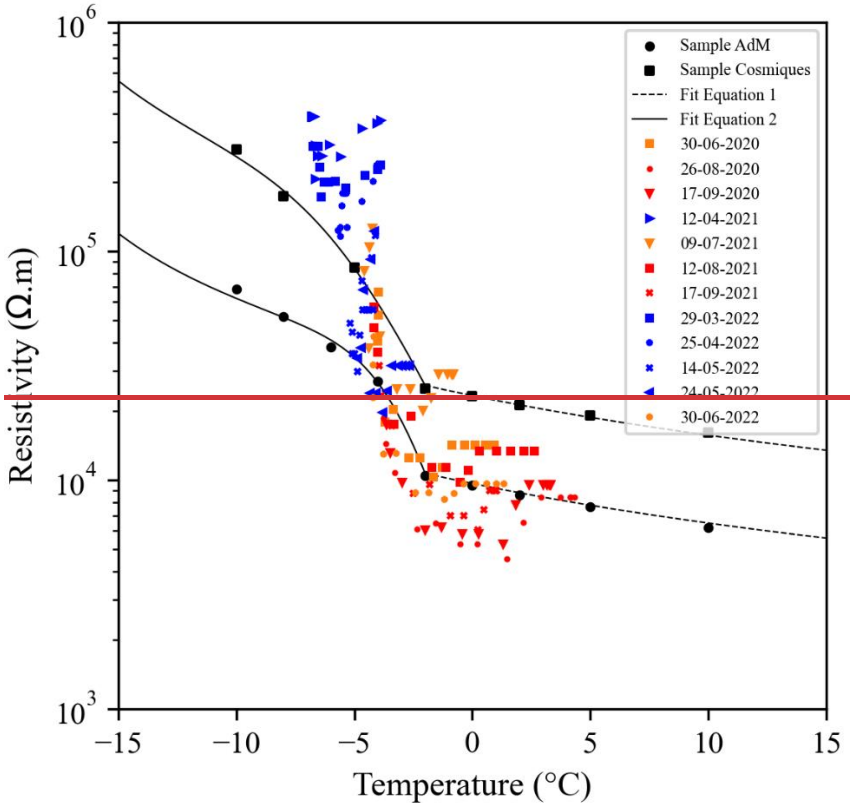

~~Figure 15. Resistivity vs. temperature. Resistivity is extracted from the tomograms in Figure 9 at location P1. Temperature is measured by sensors at BH-NW. Laboratory data on two granite samples and fitting with Equation 1 and 2 are shown too.~~

The temperatures estimation based on ERT data presented in Figures 10, led to differences of less than ±1 °C at depths 4 to 10m, indicate that the proposed model (Equation 2) can accurately reproduce the temperature in permafrost. Consequently, this approach could provide good information about the thermal distribution in the site from ERT. However, the internal temperatures of permafrost typically have just a few degrees below freezing (e.g., Noetzli et al., 2024). A precision of 1°C may be insufficient in permafrost studies, where minor temperature variations can greatly impact stability and the long-term thermal evolution.

The transition between frozen and unfrozen conditions is not clearly distinguished at resistivity curve extracted from field measurements (Fig. 9, 10). The freezing point, which is expected to result in a significant change in resistivity (as observed in laboratory measurements), does not exhibit the same effect in field. However, some datasets show gradual increase in resistivity when temperature decreased (i.e., indicating gradual freezing). This point

needs to be addressed in further research with smaller dispositive to improve the resolution of geophysical measurements.

On the south face, the tomograms show the near-surface desaturation of the pore-space attributed to the effect of the very strong insolation with a rock face that is perpendicular to the sun beam, and evidence of water infiltration along fractures (e.g., Fig. 12e, f and i). The exact pathways of infiltration and drainage are still ambiguous, possibly due to the resolution of resistivity measurements. A-ERT acquisition using shorter spacing between electrodes improves the resolution near the surface, and could provide more detailed information about the subsurface.

~~**Hydrogeological dynamics**~~

~~One of the objectives of this study was to assess the hydrogeological dynamics. While we could not precisely identify the infiltration and drainage pathways or the water table (which may be at a lower altitude), we did observe several instances that could be classified as evidence of water flux. With the AdM setting, we can hypothesize that the saturated conditions are almost never reached. There is water circulation but no accumulation of water and/or pressure because the water table is likely lower (Magnin and Josnin, 2021). As mentioned earlier, to validate these observations concerning water infiltration (e.g., Fig. 9c, l), electrical resistivity measurements should be centered around the suspected zone at the base of the central peak of the AdM. On the other hand, on the south face, the tomograms show the near-surface desaturation of the pore-space attributed to the effect of the very strong~~

~~insolation with a rock face that is perpendicular to the sun beam, and evidence of water infiltration along fractures (e.g., Fig. 11e, f and i). The exact pathways of infiltration and drainage are still ambiguous, possibly due to the resolution of resistivity measurements. A-ERT acquisition using shorter spacing between electrodes improves the resolution near the surface, and could provide more detailed information about the subsurface.~~

~~9.~~7. Conclusions

We used a repeated and ~~n~~ Automated Electrical Resistivity Tomography (A-ERT) to monitor permafrost dynamics over nearly four years at AdM in the French Alps, in order to better understand the complexities of permafrost behavior in response to climatic variations. We summarize the key findings as follow:

- ~~We highlight the critical influence of temperature on resistivity, revealing that the temperature-dependency of resistivity in field conditions is less pronounced than in controlled laboratory settings. This discrepancy could be attributed to the field's inherent heterogeneity (fractures network, infrastructures), a 3D site effect and the varying ice and water content within the rock which complicates the resistivity-temperature relationship. The results underscore the utility of ERT as a promising, non-invasive approach for monitoring permafrost evolution in high mountains, enabling the identification of permafrost~~
- Through detailed analyses of ERT data, we were able to characterize the active layer and identify significant seasonal and multiannual changes in permafrost dynamics. Importantly, we observed that the ALT varied significantly from one face to another in coherence with climate signal and measured temperatures in boreholes. The

results underscore the utility of ERT as a promising, non-invasive approach for monitoring permafrost evolution in high mountains, enabling the identification of permafrost

This research demonstrate that temperature can be accurately derived from geophysical measurements of electrical resistivity based on a petrophysical model connecting resistivity to temperature with precision of ±1 °C at depths between 4 and 10 m. We highlight the critical influence of temperature on resistivity, revealing that the temperature-dependency of resistivity in field conditions is more dispersed ~~less pronounced~~ than in controlled laboratory settings because of ~~. This discrepancy could be attributed to~~ the field's inherent heterogeneity (fractures network, infrastructures)~~, a 3D site effect and the varying ice and water content within the rock which complicates the resistivity-temperature relationship. The results underscore the utility of ERT as a promising, non-invasive approach for monitoring permafrost evolution in high mountains, enabling the identification of permafrost~~

-

- Our assessments of the hydrogeological system revealed instances of possible water flux; ~~water flux;~~ however, the exact pathways of infiltration and drainage remain unclear. Interpretation suggest that water flows detection is clearer when the site lies close to the water table allowing water column development when water infiltrates.

Although installation of A-ERT measurements system is relatively low costs, it demands substantial maintenance, especially for unstable rockwalls (where lightning effects and rockfalls led to cable problems),~~Additionally,~~ the study highlights the urgent need to address challenges related to climate conditions at high-altitudes that affect device performance and contact resistances, in order to improve the reliability of continuous A-ERT data collection.

~~Future research should focus on refining the methods for better resolving subsurface properties, particularly in areas with complex hydrological dynamics. Incorporating induced polarization measurements could enhance the interpretation of resistivity data concerning of water and ice contents.~~

Data availability. Data will be made available on request.

Author contributions. FA performed the data analysis, prepared the figures, and wrote the majority of the text. JB contributed to data acquisition, writing, and figure preparation. FM and AR contributed to the design of the ERT survey, as well as data acquisition and discussion of the results. EM, MBA and PAD contributed to the field installation and acquisition, JR conducted and processed the laboratory data, MK contributed to data inversion and discussion, TC provided air temperature data, LR and PD offered additional information about the site. Finally, all authors actively contributed to the preparation of this version of the paper.

Competing interests. The authors declare that they have no conflict of interest.

Acknowledgments. This research is part of the ANR WISPER project (ANR-19-CE01-0018) and the Action Plan on Risks from Glacial and Periglacial Origin (PAPROG) from the French Ministry of Ecological Transition, Biodiversity, Forest, Sea and Fishing. The authors acknowledge the numerous people that helped with the field work: Antoine Chabas, Bruno Galabertier and Raphaël Gallet from the EDYTEM Laboratory, Simon Alesina from the University of Lausanne, Marc Cleriot for help with field work, and Catherine Coulaud from IGE. The authors are also grateful towards the Compagnie du Mont-Blanc that provided access to the site and support.

Appendix A: Temperature measurements in boreholes on different date BH-NW and BH-S

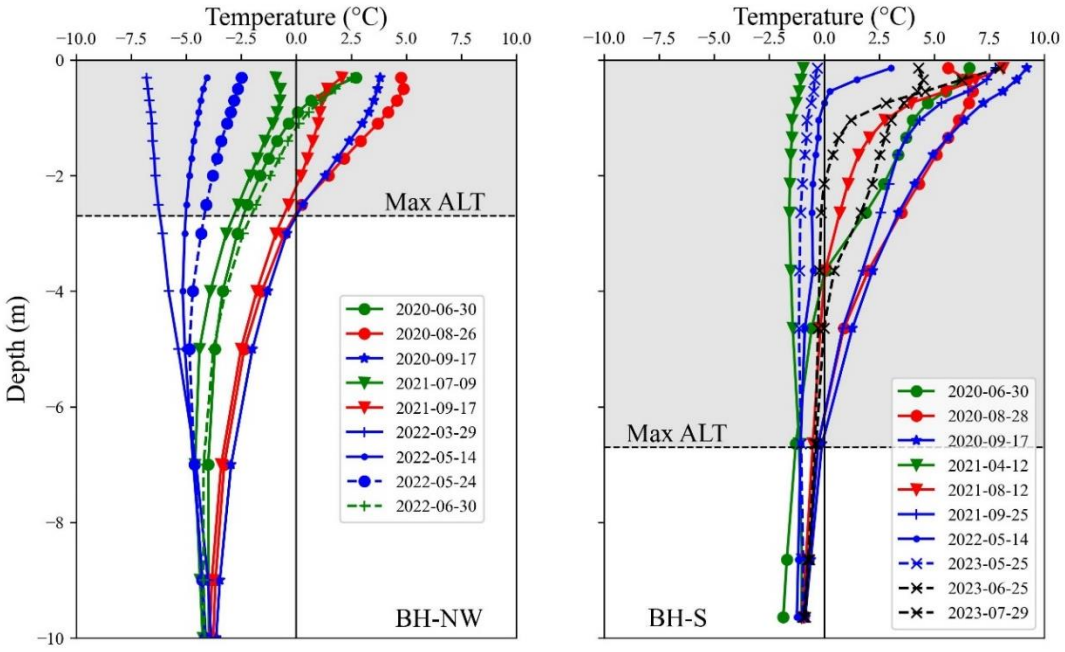

Figure A1: Temperature variation over depth in boreholes BH-NW and BH-S on different date aligned with the ERT measurement periods shown in Figure C1 and C3. The colored zones (Max ALT) indicate the maximum extent of the active layer at each borehole.

Appendix B: Evolution of the contact resistance (CR) over time at NW and S profiles.

CR measured before each daily measurement between 09/2021 and 12/2023 are presented in Figure B1.

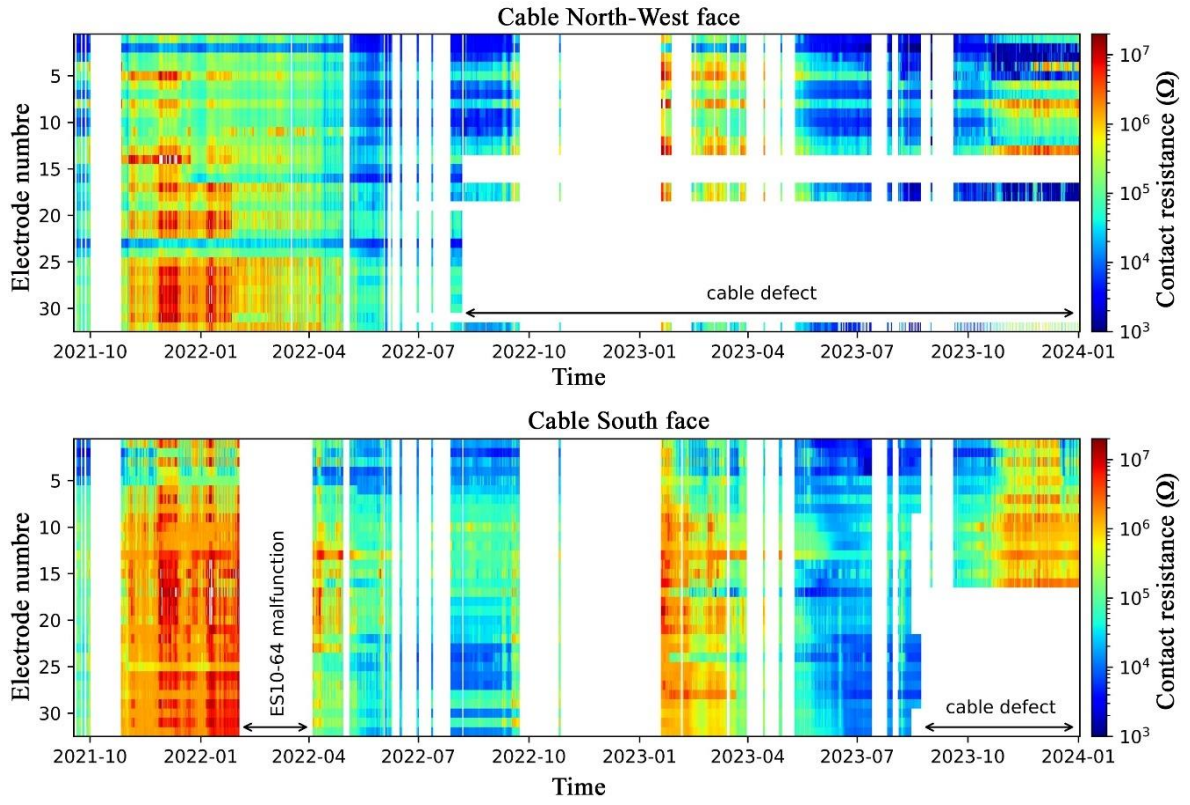

Figure B1. Temporal evolution of contact resistance at the North-West side and South side. Data partly missing are due to cable defects.

Appendix C: Summery of data presented in this study

Table 1. Summary of data presented in this study. Number of data before filtering is 155 datum points of Wenner configuration. Most of datasets has more than 80% of total number of measurements. Two datasets have more than 40% of lost data because of disconnected electrodes.

Date	N-W Profile		S Profile	
	Number of data after filter	Percentage (%)	Number of data after filter	Percentage (%)
30-06-2020	151	97.5	-	-
26-08-2020	149	96.1	90	58
17-09-2020	151	97.5	90	58
12-04-2021	118	76.1	121	78
09-07-2021	114	73.5	-	-
12-08-2021	149	96.1	140	90.3
17-09-2021	145	93.5	131	84.5
25-09-2021	143	92.2	144	92.9
29-03-2022	121	78	-	-
25-04-2022	141	91	131	84.5
14-05-2022	141	91	147	94.8
24-05-2022	140	90.3	146	94.1
30-06-2022	102	65.8	-	-
30-07-2022	-	-	145	93.5
15-08-2022	-	-	145	93.5
15-09-2022	-	-	144	93
19-03-2023	-	-	138	89
28-04-2023	-	-	143	92.2
25-05-2023	-	-	148	95.5
25-06-2023	-	-	144	92.9
29-07-2023	-	-	140	90.3

Appendix D: Time lapse inversion results

In Appendix D, we represent the time lapse inversion of a large number of datasets from north-west face and south face. The Resistivity variation ratio between consecutive electrical resistivity tomograms is also evaluated. A summary of these datasets is in table 1C.

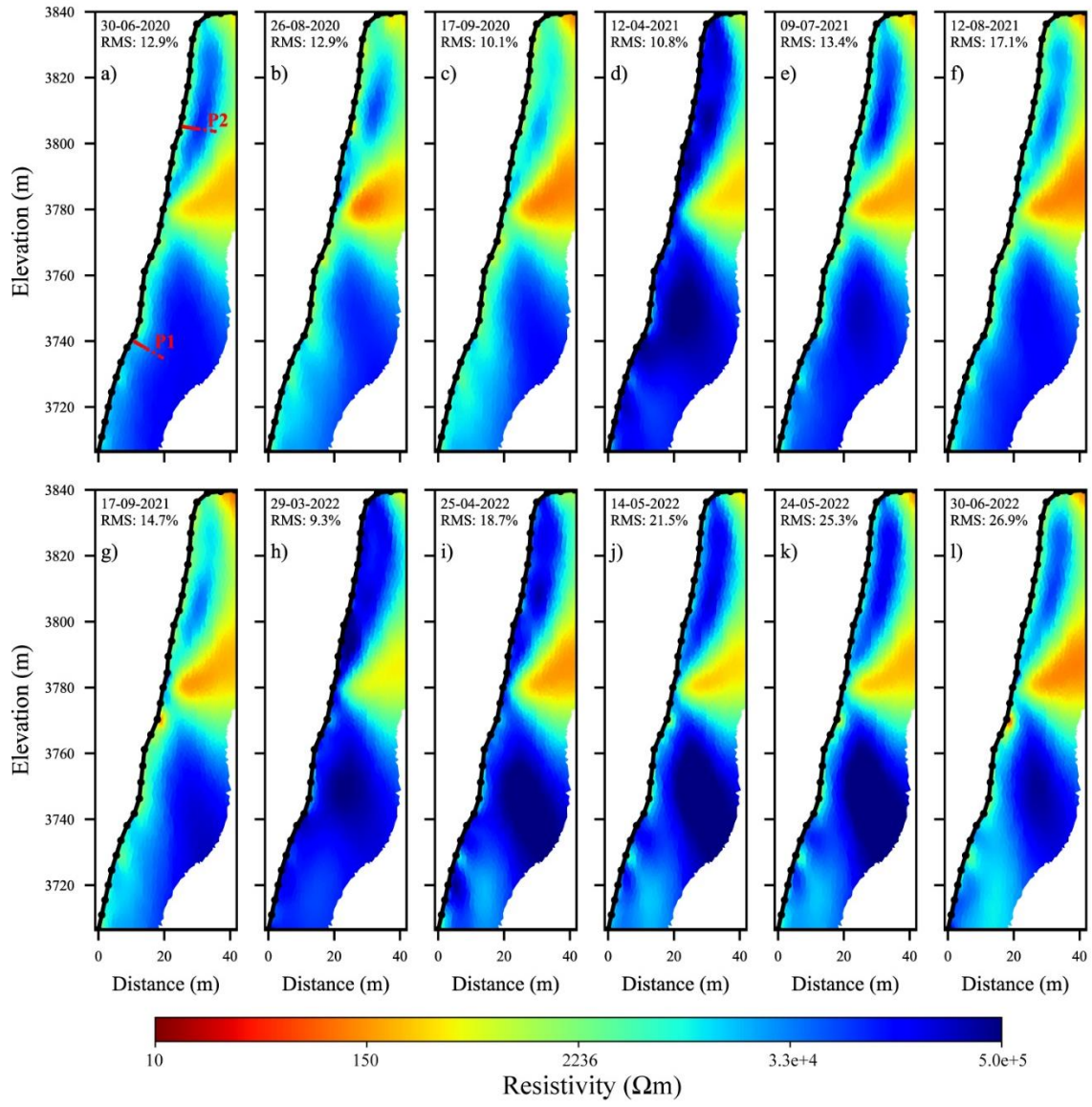

Figure D1. Electrical resistivity tomograms at different dates (from June-2020 to June-2022) along the NW side (NW profile). The conductive zone (in warm colors) denotes the presence of the gallery and elevator (see Fig. 6). The red dots (P1 in panel a) indicate the positions of the thermal sensors in the borehole BH-NW. Data presented on Figures 9 are extracted at the red dots (P1 and P2).

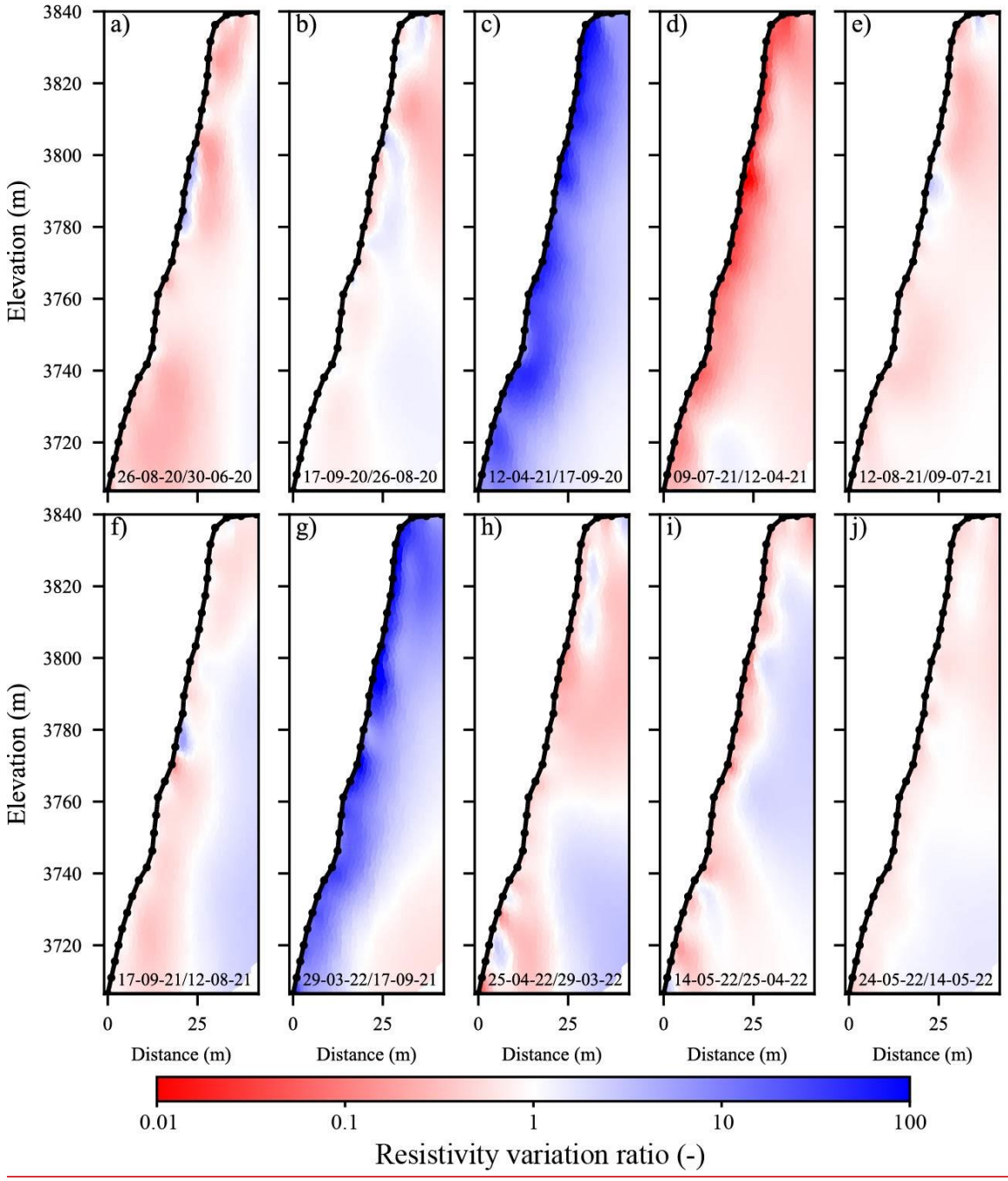

Figure D2. Resistivity variation ratio between consecutive electrical resistivity tomograms (shown in Fig. 9) along the NW side. Blue colors indicate an increase in resistivity, while red colors represent a decrease in resistivity from one measurement to the next.

Figure C3 illustrates the resistivity variation ratio between successive measurements on the S profile. The dynamics of the active layer are evident, with freezing-thawing effects visible near the surface (*e.g.*, Fig. 12a, d, and g). The heat effect (*i.e.*, decrease in resistivity values near

the surface) is more pronounced in the lower section (below the gallery). Another type of anomaly could be observed at greater depth, where heat and/or cool waves resulting of heat transfer (with delay) lead to local variations at greater depth (*e.g.*, Fig. 12d, e, g and i). In contrast, the fractured zone in the upper portion obscures the temperature dependency of resistivity due to fluctuations in air and water content (*i.e.*, resistivity in this zone is impacted by factors beyond just temperature). Water infiltration in this area could explain the rapid and significant decrease in resistivity observed between 3790 and 3820 m a.s.l. (*e.g.*, Fig. 12c, f, and j), which increases the thickness of active layer in this zone.

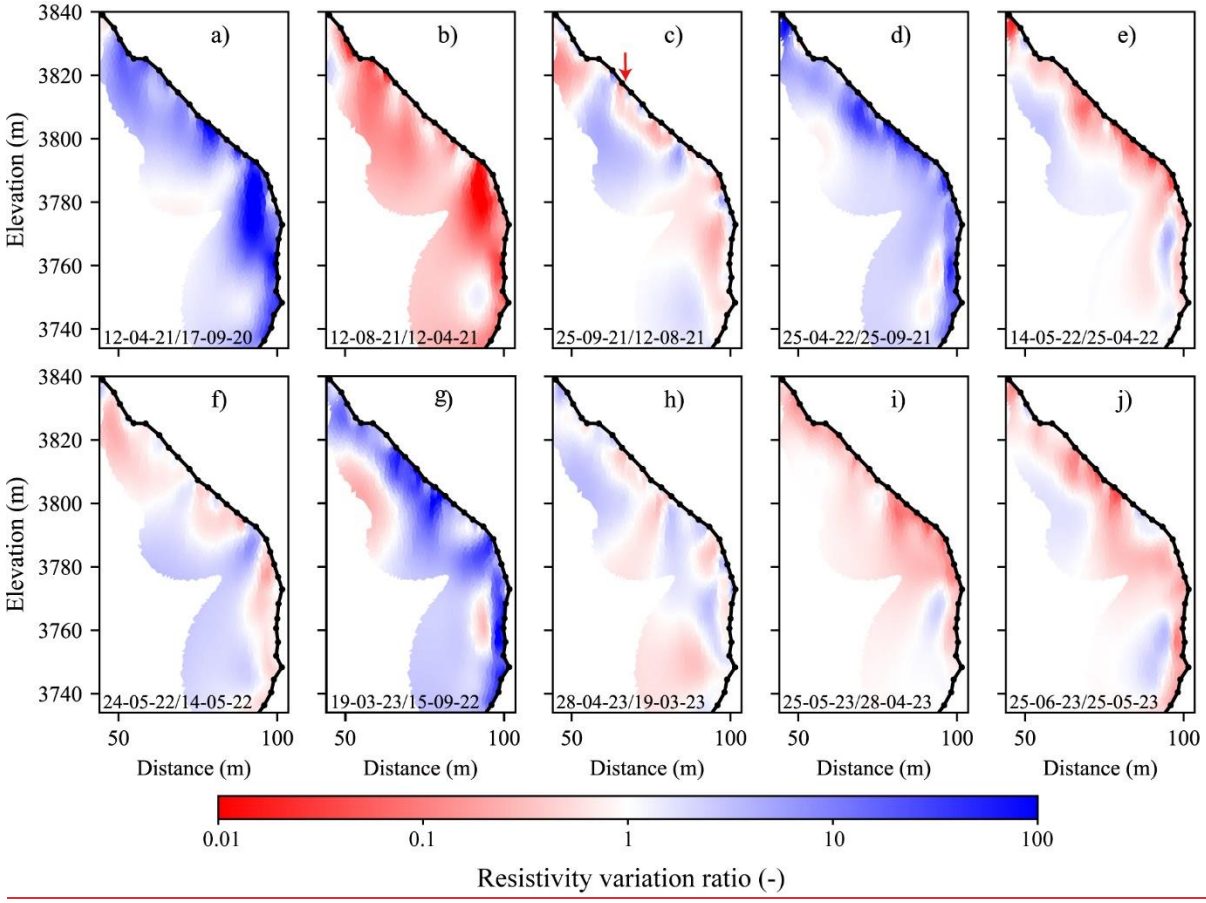

Figure D3. Resistivity variation ratio between consecutive electrical resistivity tomograms (shown in Fig. 11) along the South side. Blue colors indicate an increase in resistivity, while red colors represent a decrease in resistivity from one measurement to the next. The red arrow shows the position of possible water infiltration.

~~On the NW side (P1 and P2), the variation of resistivity with depth is more pronounced at P2, which indicates a thicker AL compared to P1. The greater thickness of AL in the upper section can be explained by the 3D heat transfer and the proximity of the shaded face (NW side) to the sun-exposed faces (S side) in the top part (Noetzli et al., 2007). In the lower section at NW side (P1 in Fig. 13), the contrast between the resistivity in the active layer and that in the permafrost (frozen zone) is not significant, which may be due to low ice content where the porosity is around 1 %, or due to high surface conductivity in granite. The alteration of granite involves the transformation of primary minerals (mica and alkali feldspars) into secondary clay minerals (such as kaolinite), which are known for their high cation exchange capacity and, consequently, their contribution to surface conductivity (Piolat et al., 2025; Revil et al., 2024). However, it is important to note that the smallest quadrupole spacing is 15 m, which is insufficient to capture thin variations close to surface (Binley and Kemna, 2005).~~

~~On the South side (the sun-exposed face), above the gallery lies the fractured zone. The extracted resistivities at P3 (Fig. 13) reveal higher values compared to the NW side (P2), showing a difference of more than one orders of magnitude at the same altitude and time. The resistivity along P3 decreases slightly with depth, indicating that almost the entirety of P3 is within the active layer. In this zone, the active layer is thicker due to the fractures, which facilitate the heat transfer and water flow. Below the gallery at P4 (Fig. 13), the active layer is more distinct compared to P1 on the NW side, displaying more pronounced variations in resistivity with depth. Below the gallery on both sides, we observe that resistivity decreased over time at greater depths (*e.g.*, at P1, comparing data from July 30, 2020 and July 30, 2022, and at P4, comparing data from April 12, 2021 and April 28, 2023), indicating degradation of the permafrost. However, this decrease in resistivity is minor because the observation period is short.~~

Furthermore, in 2021, resistivity values were higher in both the upper and lower parts compared to 2020 and 2022, and this is aligned with temperature measurements (see Fig. 2) (see details in Magnin et al. (2024)). This indicate that A-ERT is able to reveal consistent permafrost evolution.

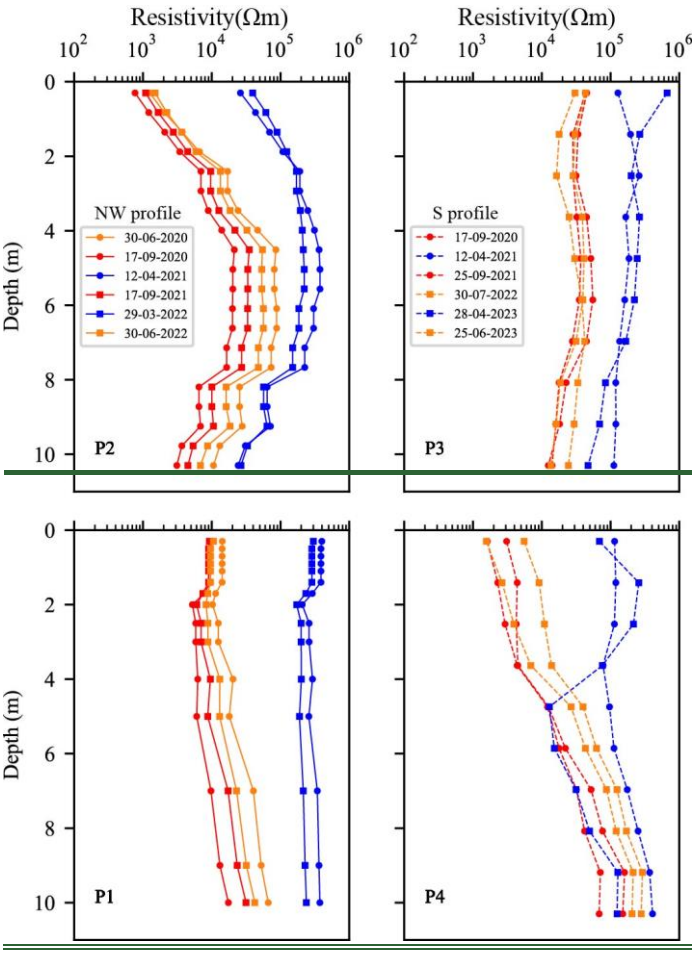

Figure 13. Resistivity extracted over depths at different locations. Resistivity extracted from tomograms on Figure 9 at P1 and P2, and from tomograms on Figure 11 at P3 and P4.

References

Abdulsamad, F., Revil, A., Ghorbani,A., Toy, V., Kirilova, M., Coperey, A., Duvillard, P. A., Ménard, G., and Ravanel, L. Complex conductivity of graphitic schists and sandstones. Journal of Geophysical Research: Solid Earth, 124, 8223‐8249. https://doi.org/10.1029/2019JB017628, 2019.

Ben-Asher, M., Magnin, F., Westermann, S., Bock, J., Malet, E., Berthet, J., Ravanel, L., and Deline, P.: Estimating surface water availability in high mountain rock slopes using a numerical energy balance model, Earth Surf. Dynam., 11, 899–915, https://doi.org/10.5194/esurf-11-899-2023, 2023.

Binley, A. and Kemna, A.: DC Resistivity and Induced Polarization Methods, in: Hydrogeophysics, Water Science and Technology Library book series, edited by: Rubin, Y. and Hubbard, S. S.,volume 50, 129‐156, https://doi.org/10.1007/1-4020-3102-5_5, 2005.

Campbell, S., Rosa T. Affleck, Sinclair, S. Ground-penetrating radar studies of permafrost, periglacial, and near-surface geology at McMurdo Station, Antarctica. Cold Regions Science and Technology, 148, Pages 38-49, https://doi.org/10.1016/j.coldregions.2017.12.008, 2018.

Cathala, M., Bock, J., Abdulsamad, F., Deline, P., Josnin, J-Y., Ravanel, L., Revil, A., Richard, J., Verroust, F., and Magnin, F. Assessing the role of permafrost in the preconditioning and triggering factors of the September 2020 Crête des Grangettes rockfall (southern French Alps), Géomorphologie: relief, processus, environnement, 30, 3, 171-188, https://doi.org/10.4000/12yqn, 2024.

Coperey, A., Revil, A., Abdulsamad, F., Stutz, B., Duvillard, P.A., and Ravanel, L. Low frequency induced polarization of porous media undergoing freezing: preliminary observations and modeling, Journal of Geophysical Research: Solid Earth, 124, doi:10.1029/2018JB017015, 2019.

Dahlin, T., and Zhou, B. A numerical comparison of 2D resistivity imaging with 10 electrode arrays, Geophys. Prospect., 52, 379–398. https://doi.org/10.1111/j.1365-2478.2004.00423.x, 2004.

Doetsch, J., Ingeman-Nielsen, T., Christiansen, A. V., Fiandaca, G., Auken, E., and Elberling, B.: Direct current (DC) resistivity and induced polarization (IP) monitoring of active layer dynamics at high

temporal resolution, Cold Reg. Sci. Technol., 119, 16–28, https://doi.org/10.1016/j.coldregions.2015.07.002, 2015.

Draebing, D. Application of refraction seismics in alpine permafrost studies: A review, Earth-Science Reviews, 155, 136–152, https://doi.org/10.1016/j.earscirev.2016.02.006, 2016.

Duvillard, P. A., Revil, A., Qi, Y., Soueid Ahmed, A., Coperey, A., and Ravanel, L.: Three-Dimensional Electrical Conductivity and Induced Polarization Tomography of a Rock Glacier, J. Geophys. Res.-Sol. Ea., 123, 9528–9554, https://doi.org/10.1029/2018JB015965, 2018.

Duvillard, P.A., Magnin, F., Revil, A., Legay, A., Ravanel, L., Abdulsamad, F., and Coperey, A.: Temperature distribution in a permafrost-affected rock ridge from conductivity and induced polarization tomography, Geophys. J. Int., 225, 1207–1221, https://doi.org/10.1093/gji/ggaa597, 2021.

Edwards, S. L.: A modified pseudosection for resistivity and IP. *Geophysics*, 42, 1020–1036, https://doi.org/10.1190/1.1440762, 1977.

Etzelmüller, B., Czekirda, J., Magnin, F., Duvillard, P.-A., Ravanel, L., Malet, E., Aspaas, A., Kristensen, L., Skrede, I., Majala, G. D., Jacobs, B., Leinauer, J., Hauck, C., Hilbich, C., Böhme, M., Hermanns, R., Eriksen, H. Ø., Lauknes, T. R., Krautblatter, M., and Westermann, S.: Permafrost in monitored unstable rock slopes in Norway – new insights from temperature and surface velocity measurements, geophysical surveying, and ground temperature modelling, Earth Surf. Dynam., 10, 97–129, https://doi.org/10.5194/esurf-10-97-2022, 2022.

~~Etzelmüller, B., Guglielmin, M., Hauck, C., Hilbich, C., Hoelzle, M., Isaksen, K., Noetzli, J., Oliva, M., and Ramos, M.Twenty years of European mountain permafrost dynamics–the PACE legacy. Environmental Research Letters, 15(10), 104070. Available from: https://doi.org/10.1088/1748-9326/abae9d, 2020.~~

Farzamian M, Vieira G, Monteiro Santos FA, et al. Detailed detection of active layer freeze-thaw dynamics using quasi-continuous electrical resistivity tomography (Deception Island, Antarctica). Cryosphere.14(3):1105-1120. https://doi.org/10.5194/tc-14-1105-2020, 2020.

Günther, T., Rücker, C., and Spitzer, K. Three-dimensional modelling and inversion of dc resistivity data incorporating topography-II. Inversion. Geophysical Journal International, Volume 166, Issue 2, August 2006, Pages 506–517, https://doi.org/10.1111/j.1365-246X.2006.03011.x, 2006.

Hartmeyer, I., Delleske, R., Keuschnig, M., Krautblatter, M., Lang, A., Schrott, L., and Otto, J.-C.: Current glacier recession causes significant rockfall increase: the immediate paraglacial response of deglaciating cirque walls, Earth Surf. Dynam., 8, 729–751, https://doi.org/10.5194/esurf-8-729-2020, 2020.

Hasler, A., Gruber. S., Font. M., and Dubois. A. Advective Heat Transport in Frozen Rock Clefts: Conceptual Model, Laboratory Experiments and Numerical Simulation, Permafrost and Periglacial Processes, 22, 378–389, https://doi.org/10.1002/ppp.737, 2011.

Hauck, C., Böttcher, M., and Maurer, H.: A new model for estimating subsurface ice content based on combined electrical and seismic data sets, The Cryosphere, 5, 453–468, https://doi.org/10.5194/tc-5-453-2011, 2011.

Hauck, C., and Hilbich C. Preconditioning of mountain permafrost towards degradation detected by electrical resistivity. Environ. Res. Lett. 19 064010. https://doi.org/10.1088/1748-9326/ad3c55, 2024.

~~Herring T, Lewkowicz AG, Hauck C, et al. Best practices for using electrical resistivity tomography to investigate permafrost. Permafrost and Periglac Process. 1-19. https://doi.org/10.1002/ppp.2207, 2023.~~

Herring, T., Lewkowicz, A. G., Hauck, C., Hilbich, C., Mollaret, C., Oldenborger, G. A., Uhlemann, S., Farzamian, M., Calmels, F., and Scandroglio, R.: Best practices for using electrical resistivity tomography to investigate permafrost, Permafrost Periglac., 34, 494–512, https://doi.org/10.1002/ppp.2207, 2023.

Hilbich, C., Marescot, L., Hauck, C., Loke, M. H., and Mäusbacher, R.: Applicability of Electrical Resistivity Tomography Monitoring to Coarse Blocky and Ice-rich Permafrost Landforms, Permafrost Periglac., 20, 269–284, https://doi.org/10.1002/ppp.652, 2009.

Hilbich, C., Hauck, C., Hoelzle, M., Scherler, M., Schudel, L., Völksch, I., Vonder Mühll, D., and Mäusbacher, R. Monitoring Mountain permafrost evolution using electrical resistivity tomography: A 7-year study of seasonal, annual, and long-term variations at Schilthorn, Swiss Alps, J. Geophys. Res.-Earth, 113, F01S90, https://doi.org/10.1029/2007JF000799, 2008.

Jacquemart, M., Weber, S., Chiarle, M., Chmiel, M., Cicoira, A., Corona, C., Eckert, N., Gaume, J., Giacona, F., Hirschberg, J., Kaitna, R., Magnin, F., Mayer, S., Moos, C., van Herwijnen, A., and Stoffel, M.: Detecting the impact of climate change on alpine mass movements in observational records from the European Alps, Earth-Science Reviews, 258, 104886, https://doi.org/10.1016/j.earscirev.2024.104886, 2024.

Karaoulis, M., Tsourlos, P., Kim, J., and Revil, A.: 4D time-lapse ERT inversion: introducing combined time and space constraints, Near Surf. Geophys., 12, 25–34, https://doi.org/10.3997/1873-0604.2013004, 2013.

Keuschnig, M., Krautblatter,M., Hartmeyer, I., Fuss, C. and Schrott, L.: Automated electrical resistivity tomography testing for early warning in unstable permafrost rock walls around Alpine infrastructure, Permafrost Periglac., ~~Process.,~~ 28, 158–171. https://doi.org/10.1002/ppp.1916, 2017.

Krautblatter, M. and Hauck, C.: Electrical resistivity tomography monitoring of permafrost in solid rock walls, J. Geophys. Res., 112, F02S20, https://doi.org/10.1029/2006JF000546, 2007.

Krautblatter M, Verleysdonk S, Flores-Orozco A., and Kemna A.: Temperature-calibrated imaging of seasonal changes in permafrost rock walls by quantitative electrical resistivity tomography (Zugspitze, German/Austrian Alps). J. Geophys. Res., ~~Earth.~~ 115, ~~(2):1-15.~~F02003, https://doi.org/10.1029/2008JF001209, 2010.

Krautblatter, M., Funk, D. and G¨unzel, F.K. Why permafrost rocks become unstable: a rock–ice-mechanical model in time and space. Earth Surf. Process. Landforms, 38, 876–887. https://doi.org/10.1002/esp.3374, 2013.

Loke, M. H. Time-lapse resistivity imaging inversion, paper presented at 5th Meeting of the Environmental and Engineering Society European Section, Budapest. 1999.

Magnin, F., Deline, P., Ravanel, L., Noetzli, J., and Pogliotti, P.: Thermal characteristics of permafrost in the steep alpine rock walls of the Aiguille du Midi (Mont Blanc Massif, 3842 m a.s.l), The Cryosphere, 9, 109–121, https://doi.org/10.5194/tc-9-109-2015, 2015b.

Magnin, F., Krautblatter, M., Deline, P., Ravanel, L., Malet, E. and Bevington, A.: Determination of warm, sensitive permafrost areas in near-vertical rockwalls and evaluation of distributed models by electrical resistivity tomography, J. geophys. Res.-Earth, 120, 745–762,- https://doi.org/10.1002/2014JF003351, 2015a.

Magnin, F., Ravanel, L., Bodin, X., Deline, P., Malet, E., Krysiecki, J.-M., et al. Main results of permafrost monitoring in the French Alps through the PermaFrance network over the period 2010–2022. Permafrost and Periglacial Processes, 35(1), 3–23. https://doi.org/10.1002/ppp.2209, 2024

Magnin, F. and Josnin, J.-Y. Water flows in Rock Wall permafrost: a numerical approach coupling hydrological and thermal processes. Journal of Geophysical Research - Earth Surface, 126(11), e2021JF006394. https://doi.org/10.1029/2021JF006394, 2021.

Maierhofer, T., Flores Orozco, A., Roser, N., Limbrock, J. K., Hilbich, C., Moser, C., Kemna, A., Drigo, E., Morra di Cella, U., and Hauck, C.: Spectral induced polarization imaging to monitor seasonal and annual dynamics of frozen ground at a mountain permafrost site in the Italian Alps, The Cryosphere, 18, 3383–3414, https://doi.org/10.5194/tc-18-3383-2024, 2024.

Mewes, B., Hilbich, C., Delaloye, R., and Hauck, C.: Resolution capacity of geophysical monitoring regarding permafrost degradation induced by hydrological processes, The Cryosphere, 11, 2957–2974, https://doi.org/10.5194/tc-11-2957-2017, 2017.

Mollaret, C., Wagner, F. M., Hilbich, C., Scapozza, C., and Hauck, C.: Petrophysical Joint Inversion Applied to Alpine Permafrost Field Sites to Image Subsurface Ice, Water, Air, and Rock Contents, Front. Earth Sci., 8, 1–25, https://doi.org/10.3389/feart.2020.00085, 2020.

Mollaret, C., Hilbich, C., Pellet, C., Flores-Orozco, A., Delaloye, R., and Hauck, C.: Mountain permafrost degradation documented through a network of permanent electrical resistivity tomography sites, The Cryosphere, 13, 2557–2578, https://doi.org/10.5194/tc-13-2557-2019, 2019.

Noetzli J., Gruber S., Kohl T., Salzmann N., Haeberli W. Three-dimensional distribution and evolution of permafrost temperatures in idealized high-mountain topography. Journal of Geophysical Research: Earth Surface 112, n/a–n/a. https://doi.org/10.1029/2006JF000545, 2007.

Noetzli, J., Isaksen, K., Barnett, J. et al. Enhanced warming of European mountain permafrost in the early 21st century. Nat Commun 15, 10508 (2024). https://doi.org/10.1038/s41467-024-54831-9.

Moser, C., Morra di Cella, U., Hauck, C., and Flores Orozco, A.: Spectral induced polarization survey for the estimation of hydrogeological parameters in an active rock glacier, The Cryosphere, 19, 143–171, https://doi.org/10.5194/tc-19-143-2025, 2025.

Offer, M., Weber, S., Krautblatter, M., Hartmeyer, I., and Keuschnig, M.: Pressurised water flow in fractured permafrost rocks revealed by borehole temperature, electrical resistivity tomography, and piezometric pressure, The Cryosphere, 19, 485–506, https://doi.org/10.5194/tc-19-485-2025, 2025.

Pavoni, M., Boaga, J., Wagner, F. M., Bast, A., Phillips, M. Characterization of rock glaciers environments combining structurally-coupled and petrophysically-coupled joint inversions of electrical resistivity and seismic refraction datasets, Journal of Applied Geophysics, 215, 0926-9851, https://doi.org/10.1016/j.jappgeo.2023.105097, 2023.

Piolat, L., Revil, A., Richard, J., Ghorbani G., Cosme, P., Géraud, Y., Casotti, C., Vaudelet, P., Diraison, M., and Favier, A., 2025.Induced polarization of volcanic rocks. 8. The case of intrusive igneous rocks. Submitted, Geophysical Journal International

Ravanel, L., Magnin, F. and Deline, P. Impacts of the 2003 and 2015 summer heatwaves on permafrost-affected rock-walls in the Mont Blanc massif. Science of the Total Environment, 609, 132–143. https://doi.org/10.1016/j.scitotenv.2017.07.055, 2017.

Revil, A., Cathles, L. M., Losh, S., & Nunn, J. A. Electrical conductivity in shaly sands with geophysical applications. Journal of Geophysical Research, 103(B10), 23,925–23,936. https://doi.org/10.1029/98JB02125, 1998.

Revil, A., Ghorbani, A., Zhao, X., Mouyeaux, A., Barrère, L., Richard, J., Peyras, L., and Vaudelet, P. Groundwater flow paths using combined self-potential, electrical resistivity, and induced polarization signals, Geophysical Journal International, 239, 2, 798–820, https://doi.org/10.1093/gji/ggae291, 2024.

Revil, A., Coperey, A., Mao, D., Abdulsamad, F., Ghorbani, A., Rossi, M., and Gasquet, D,. Induced polarization response of porous media with metallic particles — Part 8: Influence of temperature and salinity: Geophysics, 83, no. 6, E435–E456, https://doi.org/10.1190/geo2018-0089.1, 2018.

Rücker, C., Günther, T., and Wagner, F. M.: pyGIMLi: An open-source library for modelling and inversion in geophysics, Computers & Geosciences, 109, 106–123, https://doi.org/10.1016/j.cageo.2017.07.011, 2017.

Scandroglio, R., Draebing, D., Offer, M., Krautblatter, M.: 4D quantification of alpine permafrost degradation in steep rock walls using a laboratory-calibrated electrical resistivity tomography approach, Near Surface Geophys., 19,(2): 241-260, https://doi.org/10.1002/nsg.12149, 2021.

Smith, S.L., O'Neill, H.B., Isaksen, K. et al. The changing thermal state of permafrost. Nat Rev Earth Environ 3, 10–23 (2022). https://doi.org/10.1038/s43017-021-00240-1

Steiner, M., Wagner, F. M., and Flores Orozco, A.: Improved characterization of alpine permafrost through structurally constrained inversion of refraction seismic data, The Cryosphere Discuss, https://doi.org/10.5194/tc-2019-52, 2019.

Steiner, M., Wagner, F. M., Maierhofer, T., Schöner, W., and Flores Orozco, A. Improved estimation of ice and water contents in alpine permafrost through constrained petrophysical joint inversion: The Hoher Sonnblick case study," GEOPHYSICS 86: WB61-WB75. https://doi.org/10.1190/geo2020-0592.1, 2021.

Wagner, F. M., Mollaret, C., Kemna, A., and Hauck, C.: Quantitative imaging of water, ice and air in permafrost systems through petrophysical joint inversion of seismic refraction and electrical resistivity data, Geophys. J. Int., 219, 1866–1875, https://doi.org/10.1093/gji/ggz402, 2019.

Zimmermann, E., Kemna, A., Berwix, J., Glaas, W., Münch, H. M., and Huisman, J. A. A high accuracy impedance spectrometer for measuring sediments with low polarizability. Measurement Science and Technology, 19(10), 105603. https://doi.org/10.1088/0957-0233/19/10/105603, 2008.